Requirements on the gain calibration for LiteBIRD polarisation data with blind component separation

F Carralot, A Carones, N Krachmalnicoff, T Ghigna, A Novelli, L Pagano, F Piacentini, C Baccigalupi, D Adak, A Anand, et al.

▶ **To cite this version:**

F Carralot, A Carones, N Krachmalnicoff, T Ghigna, A Novelli, et al.. Requirements on the gain calibration for LiteBIRD polarisation data with blind component separation. Journal of Cosmology and Astroparticle Physics, 2025, 01, pp.019. 10.1088/1475-7516/2025/01/019 . hal-04795374

HAL Id: hal-04795374
https://hal.science/hal-04795374v1

Submitted on 17 Jan 2025

HAL is a multi-disciplinary open access archive for the deposit and dissemination of scientific research documents, whether they are published or not. The documents may come from teaching and research institutions in France or abroad, or from public or private research centers.

L'archive ouverte pluridisciplinaire **HAL**, est destinée au dépôt et à la diffusion de documents scientifiques de niveau recherche, publiés ou non, émanant des établissements d'enseignement et de recherche français ou étrangers, des laboratoires publics ou privés.

Distributed under a Creative Commons Attribution 4.0 International License

Journal of Cosmology
and Astroparticle
Physics

SISSA

PAPER • OPEN ACCESS

Requirements on the gain calibration for *LiteBIRD* polarisation data with blind component separation

To cite this article: F. Carralot *et al* JCAP01(2025)019

View the article online for updates and enhancements.

You may also like

- Impact of beam far side-lobe knowledge in the presence of foregrounds for *LiteBIRD*
C. Leloup, G. Patanchon, J. Errard et al.
- Polarization angle requirements for CMB B-mode experiments. Application to the LiteBIRD satellite
The LiteBIRD collaboration, P. Vielva, E. Martínez-González et al.
- Testing Cosmic Microwave Background Anomalies in *E*-mode Polarization with Current and Future Data
Rui Shi, , Tobias A. Marriage et al.

This content was downloaded from IP address 176.165.113.174 on 17/01/2025 at 13:18

Journal of Cosmology and Astroparticle Physics
An IOP and SISSA journal

Received: November 6, 2024
Accepted: November 17, 2024
Published: January 8, 2025

Requirements on the gain calibration for *LiteBIRD* polarisation data with blind component separation

The LiteBIRD collaboration

F. Carralot[a,b,c,*] **A. Carones**[a,c,d] **N. Krachmalnicoff**[a,c,e] **T. Ghigna**[f,g] **A. Novelli**[h] **L. Pagano**[i,j,k] **F. Piacentini**[h,l] **C. Baccigalupi**[a,c,e] **D. Adak**[m] **A. Anand**[d] **J. Aumont**[n] **S. Azzoni**[o] **M. Ballardini**[i,j,p] **A.J. Banday**[n] **R.B. Barreiro**[q] **N. Bartolo**[r,s,t] **S. Basak**[u] **A. Basyrov**[v] **M. Bersanelli**[w,x] **M. Bortolami**[i,j] **T. Brinckmann**[i] **F. Cacciotti**[h] **P. Campeti**[j,y,z] **E. Carinos**[n] **F.J. Casas**[q] **K. Cheung**[aa,ab,ac,ad] **L. Clermont**[ae] **F. Columbro**[h,l] **G. Conenna**[af] **G. Coppi**[af] **A. Coppolecchia**[h,l] **F. Cuttaia**[p] **P. de Bernardis**[h,l] **M. De Lucia**[ag] **S. Della Torre**[ah] **E. Di Giorgi**[ag] **P. Diego-Palazuelos**[y,ai] **T. Essinger-Hileman**[aj] **E. Ferreira**[g] **F. Finelli**[p,ak] **C. Franceschet**[w,x] **G. Galloni**[i,d] **M. Galloway**[v] **M. Gervasi**[af,ah] **R.T. Génova-Santos**[m,al] **S. Giardiello**[am] **C. Gimeno-Amo**[q] **E. Gjerløw**[v] **A. Gruppuso**[p,ak] **M. Hazumi**[f,an,ao,g,ap] **S. Henrot-Versillé**[aq] **L.T. Hergt**[ar] **E. Hivon**[as] **H. Ishino**[at] **B. Jost**[g] **K. Kohri**[an] **L. Lamagna**[h,l] **C. Leloup**[g] **M. Lembo**[i] **F. Levrier**[au] **A.I. Lonappan**[av] **M. López-Caniego**[aw,ax] **G. Luzzi**[ay] **J. Macias-Perez**[az] **E. Martínez-González**[q] **S. Masi**[h,l] **S. Matarrese**[r,s,t,ba] **T. Matsumura**[g] **S. Micheli**[h] **M. Monelli**[y] **L. Montier**[n] **G. Morgante**[p] **B. Mot**[n] **L. Mousset**[au,n] **Y. Nagano**[at] **R. Nagata**[ao] **T. Namikawa**[g] **P. Natoli**[i,j] **I. Obata**[g] **A. Occhiuzzi**[h] **A. Paiella**[h,l] **D. Paoletti**[p,ak] **G. Pascual-Cisneros**[q] **G. Patanchon**[bb,bc,g,bd] **V. Pavlidou**[be,bf] **G. Pisano**[h] **G. Polenta**[ay] **L. Porcelli**[bg] **G. Puglisi**[bh,bi,bj] **N. Raffuzzi**[i] **M. Remazeilles**[q] **J.A. Rubiño-Martín**[m,al] **M. Ruiz-Granda**[q,ai] **J. Sanghavi**[bk] **D. Scott**[ar] **M. Shiraishi**[bl] **R.M. Sullivan**[ar] **Y. Takase**[at] **K. Tassis**[be,bf] **L. Terenzi**[p] **M. Tomasi**[w,x] **M. Tristram**[aq] **L. Vacher**[a] **B. van Tent**[aq] **P. Vielva**[q] **G. Weymann-Despres**[aq] **E.J. Wollack**[aj] **M. Zannoni**[af,ah] **and Y. Zhou**[f]

[a] *International School for Advanced Studies (SISSA), Via Bonomea 265, Trieste 34136, Italy*
[b] *Università di Trento, Dipartimento di Fisica, Via Sommarive 14, Trento 38123, Italy*
[c] *INFN Sezione di Trieste, Via Valerio 2, Trieste 34127, Italy*
[d] *Dipartimento di Fisica, Università di Roma Tor Vergata, Via della Ricerca Scientifica 1, Roma 00133, Italy*

[*] Corresponding author.

© 2025 The Author(s). Published by IOP Publishing Ltd on behalf of Sissa Medialab. Original content from this work may be used under the terms of the Creative Commons Attribution 4.0 licence. Any further distribution of this work must maintain attribution to the author(s) and the title of the work, journal citation and DOI.

https://doi.org/10.1088/1475-7516/2025/01/019

JCAP01(2025)019

[e]IFPU, Via Beirut, 2, Grignano 34151, Trieste, Italy
[f]International Center for Quantum-field Measurement Systems for Studies of the Universe and Particles (QUP),
High Energy Accelerator Research Organization (KEK),
Tsukuba, Ibaraki 305-0801, Japan
[g]Kavli Institute for the Physics and Mathematics of the Universe (Kavli IPMU, WPI),
UTIAS, TheUniversity of Tokyo,
Kashiwa, Chiba 277-8583, Japan
[h]Dipartimento di Fisica, Università La Sapienza, P.le A. Moro 2, Roma, Italy
[i]Dipartimento di Fisica e Scienze della Terra, Università di Ferrara,
Via Saragat 1, Ferrara 44122, Italy
[j]INFN Sezione di Ferrara, Via Saragat 1, Ferrara 44122, Italy
[k]Université Paris-Saclay, CNRS, Institut d'Astrophysique Spatiale, Orsay 91405, France
[l]INFN Sezione di Roma, P.le A. Moro 2, Roma 00185, Italy
[m]Instituto de Astrofísica de Canarias, La Laguna 38200, Tenerife, Canary Islands, Spain
[n]IRAP, Université de Toulouse, CNRS, CNES, UPS, Toulouse, France
[o]Department of Astrophysical Sciences, Peyton Hall, Princeton University,
Princeton, NJ 08544, U.S.A.
[p]INAF, OAS Bologna, Via Piero Gobetti 93/3, Bologna 40129, Italy
[q]Instituto de Fisica de Cantabria (IFCA, CSIC-UC),
Avenida los Castros SN, Santander 39005, Spain
[r]Dipartimento di Fisica e Astronomia "G. Galilei", Università degli Studi di Padova,
Via Marzolo 8, Padova 35131, Italy
[s]INFN Sezione di Padova, Via Marzolo 8, Padova 35131, Italy
[t]INAF, Osservatorio Astronomico di Padova, Vicolo dell'Osservatorio 5, Padova 35122, Italy
[u]School of Physics, Indian Institute of Science Education and Research Thiruvananthapuram,
Maruthamala PO, Vithura, Thiruvananthapuram 695551, Kerala, India
[v]Institute of Theoretical Astrophysics, University of Oslo, Blindern, Oslo, Norway
[w]Dipartimento di Fisica, Università degli Studi di Milano, Via Celoria 16, Milano 20133, Italy
[x]INFN Sezione di Milano, Via Celoria 16, Milano 20133, Italy
[y]Max Planck Institute for Astrophysics, Karl-Schwarzschild-Str. 1, Garching 85748, Germany
[z]Excellence Cluster ORIGINS, Boltzmannstr. 2, Garching 85748, Germany
[aa]Jodrell Bank Centre for Astrophysics, Department of Physics and Astronomy,
School of Natural Sciences, The University of Manchester,
Alan Turing Building, Oxford Road, Manchester M13 9PL, U.K.
[ab]University of California, Berkeley, Department of Physics, Berkeley, CA 94720, U.S.A.
[ac]University of California, Berkeley, Space Sciences Laboratory, Berkeley, CA 94720, U.S.A.
[ad]Lawrence Berkeley National Laboratory (LBNL), Computational Cosmology Center,
Berkeley, CA 94720, U.S.A.
[ae]Centre Spatial de Liège, Université de Liège, Avenue du Pré-Aily, Angleur 4031, Belgium
[af]University of Milano Bicocca, Physics Department, P.zza della Scienza 3, Milan 20126, Italy
[ag]INFN Sezione di Pisa, Largo Bruno Pontecorvo 3, Pisa 56127, Italy
[ah]INFN Sezione Milano Bicocca, Piazza della Scienza 3, Milano 20126, Italy
[ai]Departamento de Física Moderna, Universidad de Cantabria,
Avda. los Castros s/n, Santander 39005, Spain
[aj]NASA Goddard Space Flight Center, Greenbelt, MD 20771, U.S.A.

JCAP01(2025)019

[ak] INFN Sezione di Bologna, Viale C. Berti Pichat 6/2, Bologna 40127, Italy
[al] Departamento de Astrofísica, Universidad de La Laguna (ULL), La Laguna 38206, Tenerife, Spain
[am] School of Physics and Astronomy, Cardiff University, Cardiff CF24 3AA, U.K.
[an] Institute of Particle and Nuclear Studies (IPNS),
High Energy Accelerator Research Organization (KEK),
Tsukuba, Ibaraki 305-0801, Japan
[ao] Japan Aerospace Exploration Agency (JAXA), Institute of Space and Astronautical Science (ISAS),
Sagamihara, Kanagawa 252-5210, Japan
[ap] The Graduate University for Advanced Studies (SOKENDAI),
Miura District, Kanagawa 240-0115, Hayama, Japan
[aq] Université Paris-Saclay, CNRS/IN2P3, IJCLab, Orsay 91405, France
[ar] Department of Physics and Astronomy, University of British Columbia,
6224 Agricultural Road, Vancouver, BC V6T1Z1, Canada
[as] Institut d'Astrophysique de Paris, CNRS/Sorbonne Université, Paris, France
[at] Okayama University, Department of Physics, Okayama 700-8530, Japan
[au] Laboratoire de Physique de l'École Normale Supérieure, ENS, Université PSL, CNRS,
Sorbonne Université, Université de Paris,
Paris 75005, France
[av] University of California, San Diego, Department of Physics, San Diego, CA 92093-0424, U.S.A.
[aw] Aurora Technology for the European Space Agency,
Camino bajo del Castillo s/n, Urbanización Villafranca del Castillo, Villanueva de la Cañada,
Madrid, Spain
[ax] Universidad Europea de Madrid, Madrid 28670, Spain
[ay] Space Science Data Center, Italian Space Agency, Via del Politecnico, Roma 00133, Italy
[az] Université Grenoble Alpes, CNRS, LPSC-IN2P3, 53, avenue des Martyrs, Grenoble 38000, France
[ba] Gran Sasso Science Institute (GSSI), Viale F. Crispi 7, L'Aquila 67100, Italy
[bb] ILANCE, CNRS, University of Tokyo International Research Laboratory,
Kashiwa, Chiba 277-8582, Japan
[bc] Université Paris Cité, Paris 75006, France
[bd] Université Paris Cité, CNRS, Astroparticule et Cosmologie, Paris 75013, France
[be] Institute of Astrophysics, Foundation for Research and Technology,
Vasilika Vouton 70013, Heraklion, Greece
[bf] Department of Physics and ITCP, University of Crete, Heraklion 70013, Greece
[bg] Istituto Nazionale di Fisica Nucleare-Laboratori Nazionali di Frascati (INFN-LNF),
Via E. Fermi 40, Frascati 00044, Italy
[bh] Dipartimento di Fisica e Astronomia, Università degli Studi di Catania,
Via S. Sofia 64, Catania 95123, Italy
[bi] INAF, Osservatorio Astrofisico di Catania, Via S. Sofia 78, Catania 95123, Italy
[bj] INFN, Sezione di Catania, Via S. Sofia 64, Catania 95123, Italy
[bk] Universitäts Sternwarte München, Ludwig-Maximilians-Universität München,
Scheinerstr. 1, München 81679, Germany
[bl] Suwa University of Science, Chino, Nagano 391-0292, Japan

E-mail: fcarralo@sissa.it

Abstract: The detection of primordial B modes of the cosmic microwave background (CMB) could provide information about the early stages of the Universe's evolution. The faintness of this signal requires exquisite calibration accuracy and control of instrumental systematic

JCAP01(2025)019

effects which otherwise could bias the measurements. In this work, we study the impact of an imperfect relative polarisation gain calibration on the recovered value of the tensor-to-scalar ratio r for the *LiteBIRD* experiment, through the application of the blind Needlet Internal Linear Combination (NILC) foreground-cleaning method. We derive requirements on the relative calibration accuracy of the overall polarisation gain (Δg_ν) for each *LiteBIRD* frequency channel. Our results show that minimum variance techniques, as NILC, are less sensitive to systematic gain calibration uncertainties compared to a parametric approach, if the latter is not equipped with a proper modelling of these instrumental effects. In this study, the most stringent requirements are found in the channels where the CMB signal is relatively brighter, with the tightest constraints at 166 GHz ($\Delta g_\nu \approx 0.16\%$). This differs from the outcome of an analogous analysis performed with a parametric method, where the tightest requirements are obtained for the foreground-dominated channels. Gain calibration uncertainties, corresponding to the derived requirements, are then simultaneously propagated into all frequency channels. By doing so, we find that the overall impact on estimated r is lower than the total gain systematic budget for *LiteBIRD* approximately by a factor 5, due to the correlations of the impacts of gain calibration uncertainties in different frequency channels. In order to decouple the systematic effect from the specific choice of the model, we derive the requirements assuming constant spectral parameters for the foreground emission. To assess the robustness of the obtained results against more realistic scenarios, we repeat the analysis assuming sky models of intermediate and high complexity. In these further cases, we adopt an optimised NILC pipeline, called the Multi-Clustering NILC (MC-NILC). We find that the impact of gain calibration uncertainties on r is lower than the *LiteBIRD* gain systematics budget for the intermediate-complexity sky model. For the high-complexity case, instead, it would be necessary to tighten the requirements by a factor 1.8.

Keywords: CMBR experiments, CMBR polarisation

ArXiv ePrint: 2411.02080

JCAP01(2025)019

Contents

JCAP01(2025)019

1 Introduction

Measurements of temperature anisotropies of the Cosmic Microwave Background (CMB) [1] by the *COBE* [2], *WMAP* [3] and *Planck* [4–6] spacecraft and BOOMERanG [7], SPT [8] and ACT [9] among other sub-orbital experiments[1] led to major advancements in cosmology, allowing us to precisely constrain cosmological parameters in models capable of describing the evolution of the Universe. In the last decade, efforts have been focused on the analysis of the CMB polarisation signals, which could serve as an additional observational window into the early Universe. Indeed, the standard model of Cosmology predicts that the Universe experienced a phase of exponential expansion perhaps 10^{-36}–10^{-34} s after the Big Bang, named *cosmic inflation* [10]. Such expansion magnified quantum fluctuations to cosmological scales and also generated tensor perturbations that produce a specific signature in the CMB polarisation: the B-mode pattern [11–13]. Therefore, the detection of primordial CMB B modes could enable the estimation of the amplitude of primordial gravitational waves quantified by the tensor-to-scalar ratio parameter r [14] and potentially confirm the inflationary scenario. Due to the expected amplitude of such a signal (at least 1000 times weaker than temperature anisotropies), primordial B modes have not been detected yet, with current upper bounds on the tensor-to-scalar ratio $r \lesssim 0.03$ (95% CL) [15, 16]. Their detection thus represents one of the main goals of future CMB missions. In order to probe the inflationary paradigm, it is essential to target large angular scales by measuring two main

[1] https://lambda.gsfc.nasa.gov/.

power spectrum features: the reionisation bump ($\ell \lesssim 10$), associated with the scattering of CMB photons with free electrons released during cosmic reionisation, and the recombination bump ($\ell \sim 80$) [17, 18], which instead corresponds to the imprint of primordial tensor perturbations at the recombination epoch. On smaller angular scales, CMB B modes are also generated from lensed CMB polarisation E modes due to the gravitational interaction of CMB photons with the intervening cosmic large scale structure [19, 20]. Such a signal has already been measured by SPTpol [21], ACTpol [22], PolarBear [17] and BICEP2/Keck [18] ground based experiments.

Despite huge progress in terms of instrumental sensitivity, detecting primordial B modes still remains extremely challenging. One of the major impediments for an accurate measurement of the CMB polarisation signal is the contamination due to Galactic emission [23]. Physical processes occurring within our Galaxy induce complex emission, that is challenging to model and that must be subtracted for any scientific exploitation of CMB data. In the framework of CMB polarisation analysis, we can safely neglect some Galactic microwave radiative processes like free-free radiation [24, 25], anomalous microwave emission (AME) [26–29] or CO molecular lines [30], since they are characterised by a very low polarisation fraction ($\lesssim 1\%$), and hence we need to consider only synchrotron and thermal dust polarised emission [31, 32]. The synchrotron radiation, that is dominant at low frequencies ($\lesssim 70\,\mathrm{GHz}$), is generated by cosmic-ray electrons that are accelerated by the Galactic magnetic field. At high frequencies ($\gtrsim 100\,\mathrm{GHz}$), aspherical dust grains in the interstellar medium are heated by stellar ultraviolet radiation and re-emit far-infrared radiation with a polarisation fraction close to 20%. These two emission mechanisms are obviously prominent around the Galactic plane, but are also clearly detectable at higher latitudes [33]. In the context of the *Planck* mission, various foreground cleaning procedures have been employed [34]. Among them, we mention two categories: (i) parametric-fitting [35–40], which recovers the CMB signal by marginalising over the spectral parameters of Galactic foregrounds; and (ii) the so-called 'blind' methods [41–45], whose purpose is to recover a cleaned CMB blackbody signal, without any assumption on the spectral energy distribution (SED) of foreground emission. Methods of the latter class, in most cases, are also referred to as *minimum-variance* techniques, since they reconstruct the CMB signal as the minimum variance solution from the linear combination of multi-frequency observations, thus maximally reducing the foreground contamination in the 2-point statistics [46].

The second main source of uncertainty is the presence of instrumental systematic effects, arising from non-idealities and imperfect characterisation of the instrument. As mentioned above, the weak amplitude of the B-mode signal requires an exquisite degree of control of both polarised Galactic emission and systematic effects. Therefore, it is essential to develop techniques that are able to handle multiple sources of uncertainty that could lead to biases in the reconstructed primordial B modes.

Among future CMB experiments, *LiteBIRD* [47–49] (Lite (Light) satellite for the studies of B-mode polarisation and Inflation from cosmic background Radiation Detection), is a space-borne experiment selected by the Japanese Aerospace Exploration Agency (JAXA) and which is currently backed by a world-wide collaboration. *LiteBIRD* will perform 3 years of full-sky observations to target an overall uncertainty on the tensor-to-scalar ratio of $\sigma_r \leq 10^{-3}$ by measuring both the recombination and reionisation bumps. The scope of this paper is to

JCAP01(2025)019

study the impact of imperfect photometric gain calibration on the estimate of the tensor-to-scalar ratio for the *LiteBIRD* experiment. Therefore, in this paper, we set requirements on the gain calibration accuracy for each of *LiteBIRD*'s frequency channels, which will allow it to fulfill the budget allocated to gain systematics, $\Delta r = 6.5 \times 10^{-6}$ [48]. In this work, we refer to the relative polarisation gain as the gain calibration of polarisation data (Q and U Stokes parameter maps) relative to a specific frequency channel. In practice, this corresponds to the product of the intensity calibration and polarisation efficiency. The absolute gain, which is associated with a common amplitude factor affecting all frequency channels, does not impact the component-separation outcome and therefore we do not consider it in our analysis.

In this work, we make use of Needlet Internal Linear Combination (NILC) [50, 51], a blind component-separation technique that performs a linear combination of frequency maps in needlet space, in order to minimise the variance of the final map separately at different angular scales. The choice of using a blind component-separation method is motivated by an analogous study in [52], which derive the requirements on the gain calibration for *LiteBIRD* considering the parametric fitting `FGBuster`[2] pipeline. This latter analysis finds stringent requirements on the gain, especially for synchrotron- and dust-dominated frequencies. Indeed, gain calibration uncertainties induce distortions in the foreground SEDs, which, if not adequately captured and described by the parametric modelling, bias the reconstructed CMB signal. Therefore, the parametric methods require a specific implementation to be able to marginalise over instrumental systematic effects. As an example, the `Commander` [53] pipeline, (largely adopted for the analysis of *Planck* data) jointly fits the foreground and instrumental parameters, thus being able to mitigate the impact of gain uncertainties on component-separation products. Since, as previously mentioned, the constraints on the gain calibration obtained in [52] appeared to be tight, we consequently aim to reproduce the procedure presented in [52] to set requirements on the gain calibration using the NILC minimum-variance component separation. Specifically, we are interested in assessing to what extent the choice of a specific component-separation method affects the estimation of the tensor-to-scalar ratio in the presence of gain calibration uncertainties.

The paper is structured as follows. In section 2, we outline the procedure to generate sky maps for each frequency of the *LiteBIRD* satellite and to simulate the effect of an imperfect gain calibration. Section 3 describes the NILC foreground cleaning method, its importance for studies of systematic effects and the specific algorithmic choices made for this analysis. The procedure to estimate the tensor-to-scalar ratio from cleaned CMB maps and to set requirements on the gain calibration are explained in sections 4 and 5, respectively. The results of this analysis are then presented in section 5. In section 6, we summarise our main results and comment on future work.

2 Simulation pipeline

In this section we describe our simulation framework. This includes the modelling of the sky emission, the generation of realistic observations by the instrument and the injection of relative polarisation gain uncertainty in the simulated maps.

[2] https://github.com/fgbuster/fgbuster.

JCAP01(2025)019

2.1 Instrument model

Contamination by Galactic emission demands that we consider observations over a broad frequency range. Therefore, *LiteBIRD* is composed of three instruments: the Low Frequency Telescope [54] (LFT); the Medium Frequency Telescope (MFT); and the High Frequency Telescope (HFT) [55]. The LFT is designed to observe CMB and synchrotron emission between 34 and 161 GHz over 12 frequency channels. The MFT and HFT instruments (the so-called MHFT) will observe in the frequency ranges 89–224 and 166–448 GHz, respectively. Such frequency coverage is designed to characterise the dust emission and increase the sensitivity in the CMB channels, corresponding to the frequency range $90 \lesssim \nu \lesssim 140$ GHz. *LiteBIRD* will operate with angular resolution ranging between 24 and 71 arc-minutes in order to cover the multipole range $2 \lesssim \ell \lesssim 300$ of the CMB B-mode angular power spectrum. The instrumental specifications used in this analysis are reported in table 1.

The first optical element of each telescope is a rotating half-wave plate (HWP) as polarisation modulator. The HWP's purpose is to reduce the contribution of $1/f$ noise and mitigate some other systematic effects such as gain drifts or intensity-to-polarisation leakage [48]. The full description of the real behaviour of the HWP is subject to uncertainties that contribute to the total systematic budget [56–58]. However, since we aim to assess the impact of gain calibration uncertainties only, we assume an ideal polarisation modulator that does not generate additional systematic artefacts.

2.2 Sky model

The total sky emission is given by the superposition of the CMB and Galactic signals. As mentioned in section 1, we consider only polarised dust and synchrotron emission. Polarised dust emission is modelled with a modified blackbody SED [31]:

$$[I, Q, U]_{\rm dust} = A_{[I,Q,U]_{\rm dust}} \left(\frac{\nu}{\nu_{\rm ref}}\right)^{\beta_{\rm d}} \frac{B(\nu, T_{\rm d})}{B(\nu_{\rm ref}, T_{\rm d})}\,, \tag{2.1}$$

with $\beta_{\rm d}$ the dust spectral index, $B(\nu, T)$ the blackbody spectrum, $T_{\rm d}$ the dust temperature, and ν the frequency. The quantity $\nu_{\rm ref}$ corresponds to the pivot frequency, which allows us to define a reference template $A_{[I,Q,U]}$ for polarised dust.

Synchrotron emission can be modelled with a power-law spectrum [59]:

$$[I, Q, U]_{\rm syn} = A_{[I,Q,U]_{\rm syn}} \left(\frac{\nu}{\nu_{\rm ref}}\right)^{\beta_{\rm s}}\,, \tag{2.2}$$

with $\beta_{\rm s}$ the spectral index of synchrotron, $\nu_{\rm ref}$ a pivot frequency, and $A_{[I,Q,U]_{\rm syn}}$ the synchrotron emission template at frequency $\nu_{\rm ref}$.

In this analysis, we simulate synchrotron and dust maps at each *LiteBIRD* frequency assuming the `s0` and `d0` emission models, as implemented in the `PySM`[3] package. In these models, both polarised dust and synchrotron spectral parameters are uniform across the sky and equal to $\beta_{\rm s} = -3$, $\beta_{\rm d} = 1.54$, and $T_{\rm d} = 20\,{\rm K}$. Such values correspond to a sky-average of the spectral parameters as fitted to *WMAP* and *Planck* data [31, 60]. Although it is well-known that foreground spectral parameters vary across the sky [31, 61, 62], we

[3] https://pysm3.readthedocs.io/.

JCAP01(2025)019

Instrument	ν [GHz]	Channel label	Beam FWHM [arcmin]	Sensitivity [μK-arcmin]	$N_{\rm bol}$
LFT	40	LFT-40	70.5	37.42	48
	50	LFT-50	58.5	33.46	24
	60	LFT-60	51.1	21.31	48
	68	LFT-68a	41.6	19.91	144
	68	LFT-68b	47.1	31.77	24
	78	LFT-78a	36.9	15.55	144
	78	LFT-78b	43.8	19.13	48
	89	LFT-89a	33.0	12.28	144
	89	LFT-89b	41.5	28.77	24
	100	LFT-100	30.2	10.34	144
	119	LFT-119	26.3	7.69	144
	140	LFT-140	23.7	7.25	144
MFT	100	MFT-100	37.8	8.48	366
	119	MFT-119	33.6	5.70	488
	140	MFT-140	30.8	6.38	366
	166	MFT-166	28.9	5.57	488
	195	MFT-195	28.0	7.05	366
HFT	195	HFT-195	28.6	10.50	254
	235	HFT-235	24.7	10.79	254
	280	HFT-280	22.5	13.80	254
	337	HFT-337	20.9	21.95	254
	402	HFT-402	17.9	47.45	338

Table 1. *LiteBIRD* instrumental specifications. From left to right: the instrument; the frequency channel and its label; the beam full width at half maximum (FWHM); the polarisation sensitivity; and the number of bolometers.

adopt this simplified sky model to: (i) disentangle the impact of the complexity of the sky model from that of the systematic effect under study and (ii) match the foreground model used in [52], to compare the impact of gain calibration uncertainties on different component-separation approaches.

The CMB component is generated from the *Planck* best-fit angular power spectrum [63] using the Code for Anisotropies of Microwave Background `CAMB`[4] [64] with the following set of cosmological parameters: $r = 0$, $A_{\rm s} = 2 \times 10^{-9}$, $n_{\rm s} = 0.965$ and $\tau = 0.06$ with $A_{\rm s}$ and $n_{\rm s}$, respectively, being the amplitude and spectral index of the power spectrum of primordial scalar fluctuations and the parameter τ being the reionisation optical depth. In addition to CMB and Galactic emission, we generate realisations of instrumental noise. This latter is assumed to be white, isotropic and uncorrelated between frequency channels. We recall that

[4] https://camb.readthedocs.io/.

JCAP01(2025)019

the contribution of $1/f$ noise is negligible, since we assume an ideal HWP that fully mitigates this effect. We produce noise realisations for each frequency band using the polarisation sensitivity values reported in table 1. For each *LiteBIRD* channel, the simulated CMB, synchrotron and dust maps are smoothed with the corresponding Gaussian FWHM shown in table 1 and then coadded together with a noise realisation. We finally bring all frequency maps to *LiteBIRD*'s lowest angular resolution: $70.5'$.

Following this procedure, we thus obtain 22 polarisation Stokes Q and U maps with a common angular resolution of $70.5'$. We do not integrate over the bandwidth, thus having monochromatic maps. The choice of not adopting realistic bandpasses is motivated by the fact that it does not have any relevant impact on the employed blind component-separation approach. The NILC algorithm demands input maps to be scalar, therefore we convert the obtained polarisation full-sky Q and U maps into E- and B-mode maps. A detailed description of this transformation is presented in [65]. We focus our analysis on B-mode maps, since we aim to assess the impact of the polarisation gain mis-calibration on the measurement of the tensor-to-scalar ratio.

2.3 Simulating the relative polarisation gain mis-calibration

To introduce a gain calibration uncertainty, we adopt a simple framework in which each frequency map is multiplied by a frequency-dependent gain calibration factor g_ν assumed to be homogeneous and constant over time. The total signal at a given frequency, d_ν^B, can be thus expressed in the following way:

$$d_\nu^B = g_\nu (m_{\nu,\mathrm{cmb}}^B + m_{\nu,\mathrm{fg}}^B + n_\nu)\,, \tag{2.3}$$

where $m_{\nu,\mathrm{cmb}}^B$ and $m_{\nu,\mathrm{fg}}^B$ represent the CMB and foreground B-mode maps, respectively, while n_ν is the white noise. In the case of a perfect gain calibration, $g_\nu = 1$ for each frequency ν. To simulate the relative calibration error, we generate, for each channel, a random value of g_ν from a Gaussian distribution with standard deviation Δg_ν:

$$g_\nu = 1 + \mathcal{N}(0, \Delta g_\nu). \tag{2.4}$$

Throughout this paper, the g_ν calibration factors are sampled from the Gaussian distribution shown in eq. (2.4) and the gain uncertainty Δg_ν, setting the width of this distribution, is the parameter on which we aim to derive a requirement.

3 Component-separation algorithm

In this work, as anticipated in section 1, we adopt the NILC pipeline to recover CMB B modes from *LiteBIRD* multifrequency simulated data. Such a method has already been largely employed in CMB data analysis, e.g. for *WMAP* [50] and *Planck* [34], and it will also be one of the foreground cleaning pipelines for other next-generation CMB experiments, such as Simons Observatory [66].

NILC falls in the category of blind component-separation methods, since it performs a reconstruction of the CMB signal without any assumptions on the foreground spectral properties. It thus represents a valuable alternative to parametric approaches, as it is not

JCAP01(2025)019

affected by spectral mismodelling of the Galactic polarised emission, which may significantly bias the final estimate of the tensor-to-scalar ratio. Moreover, previous studies [67] have shown that ILC techniques, such as NILC, are only mildly affected by calibration errors in the low signal-to-noise regime, as will be the case for CMB B-mode reconstruction with all upcoming experiments. Therefore, NILC is expected to represent the optimal framework to build a reliable reconstruction of CMB B modes with less restrictive requirements for *LiteBIRD* on gain calibration uncertainties as appeared to be the case for those obtained in [52]. We thus apply NILC to the mis-calibrated maps (described in section 2.3) and set requirements on the Δg_ν parameter for each frequency channel ν, by checking its impact on the retrieved CMB B-mode solution and the tensor-to-scalar ratio estimation.

3.1 Mathematical formalism

The ILC approach consists of reconstructing a cleaned CMB signal by linearly combining input data at different frequencies with frequency-dependent weights:

$$\tilde{X}_{\rm CMB} = \sum_{\nu=1}^{N_\nu} \omega_\nu X^\nu = \sum_{\nu=1}^{N_\nu} \omega_\nu (a^\nu_{\rm CMB} X_{\rm CMB} + X^\nu_{\rm fg} + X^\nu_{\rm n}) \,, \tag{3.1}$$

with X^ν representing the input observations at frequency ν in a specific domain, $a^\nu_{\rm CMB}$ the CMB SED and $a^\nu_{\rm CMB} X_{\rm CMB}$, $X^\nu_{\rm fg}$ and $X^\nu_{\rm n}$ the corresponding CMB, foregrounds and instrumental noise contributions, respectively. The optimal weights ω_ν are estimated with the constraint of preserving the CMB blackbody signal:

$$\sum_{\nu=1}^{N_\nu} \omega_\nu a^\nu_{\rm CMB} X_{\rm CMB} = X_{\rm CMB} \,, \tag{3.2}$$

and to minimise the output variance $\mathrm{Var}(\tilde{X}_{\rm CMB})$.

In pixel-based and harmonic ILC, X^ν corresponds, respectively, to input B-mode maps and harmonic coefficients [46, 68]. Therefore, in these cases, the variance minimisation accounts for either the full range of angular scales or all directions on the sky. However, the relative contribution of Galactic emission and instrumental noise is expected to vary across the sky and among multipole moments. It follows that the subtraction of contaminants in the recovered CMB B modes can be augmented through a variance minimisation performed locally in both domains. This is implemented in NILC, which extends the ILC approach to the needlet domain [41, 50]. Needlets are a specific wavelet system that guarantees simultaneous localisation of the deprojected field in both real and harmonic space. In practice, needlet deprojection of a B-mode map at frequency ν, d^B_ν, returns a set of needlet maps, β^ν_j, obtained by filtering its harmonic coefficients, $a^B_{\ell m,\nu}$, with different harmonic window functions $b_j(\ell)$:

$$\beta^\nu_j(\hat{\gamma}) = \sum_{\ell,m} \left[a_{\ell m,\nu} b_j(\ell) \right] Y_{\ell m}(\hat{\gamma}) \,, \tag{3.3}$$

with $\hat{\gamma}$ a specific direction on the sky and j the needlet scale. For each j, we sample a specific range of multipole moments, with lower values of j corresponding to ranges of larger angular scale. The total number of needlet scales N_j depends on the targeted resolution for the reconstruction of the CMB signal. The procedure outlined in eq. (3.3) is equivalent to a

JCAP01(2025)019

convolution of d_ν^B with N_j different kernels associated with the needlet filters $b_j(\ell)$. Since such filters are band-limited, each needlet coefficient $\beta_j^\nu(\hat{\gamma})$ is only sourced by modes of d_ν^B in a specific range of angular scales and within a finite spatial domain around $\hat{\gamma}$. Therefore, in NILC the input needlet maps are linearly combined separately for each needlet scale j:

$$\beta_j^{\rm NILC}(\hat{\gamma}) = \sum_{\nu=1}^{N_\nu} \omega_\nu^j(\hat{\gamma})\beta_j^\nu(\hat{\gamma}) = \sum_{\ell,m} a_{\ell m,j}^{\rm NILC} Y_{\ell m}(\hat{\gamma})\,, \tag{3.4}$$

so as to locally minimise the variance of $\beta_j^{\rm NILC}(\hat{\gamma})$, thus effectively reducing the contamination locally in both pixel and multipole domains. The NILC weights, $\omega_\nu^j(\hat{\gamma})$, can be easily computed from the input needlet covariance $C_{\nu\mu}^{(j)}(\hat{\gamma}) = \langle\beta_j^\nu(\hat{\gamma})\beta_j^\mu(\hat{\gamma})\rangle$:

$$\omega_\nu^j(\hat{\gamma}) = \frac{a_{\rm CMB}^\mu\left(C_{\nu\mu}^{(j)-1}(\hat{\gamma})\right)}{a_{\rm CMB}^\mu\left(C_{\nu\mu}^{(j)-1}(\hat{\gamma})\right)a_{\rm CMB}^\nu}. \tag{3.5}$$

We can immediately observe that the estimation of NILC weights does not require any modelling or a priori knowledge of foreground spectral properties. In the baseline NILC analysis, the sample average in the covariance computation is performed within Gaussian axisymmetric domains (whose size varies with the considered needlet scale) centred around each sky direction. This is the approach adopted in this work. If the Galactic emission turns out to be very complex, the choice of such domains can be optimised through taking into account a data-driven blind estimation of the spatial distribution of the spectral properties of Galactic B-mode foregrounds, as implemented in Multiclustering-NILC [45].

Once the output variance is separately minimised at the different needlet scales through eq. (3.4), the final NILC CMB B-mode map is obtained by performing an inverse needlet transformation of the needlet solutions $\beta_j^{\rm NILC}$. In practice, this is done by first convolving each $\beta_j^{\rm NILC}$ by the corresponding kernel (associated with $b_j(\ell)$) and then summing all the obtained maps at the different needlet scales:

$$B_{\rm CMB}^{\rm NILC} = \sum_j \sum_{\ell,m} \left[a_{\ell m,j}^{\rm NILC} b_j(\ell)\right] Y_{\ell m}(\hat{\gamma}). \tag{3.6}$$

By looking at the direct and inverse needlet transformations of eqs. (3.3) and (3.6), it follows that $\sum_j b_j^2(\ell) = 1$ for each multipole moment.

3.2 NILC implementation in our framework

In this section, we provide details of the specific NILC configuration employed in this work. The main feature is the analytical form of the needlet functions $b_j(\ell)$. Commonly adopted constructions are the *standard* [69, 70], the *cosine* [50] and the *Mexican-hat* needlets [71]. In this analysis we adopt Mexican needlets generated with the Python module `MTNeedlet`.[5] The Mexican needlet bands are Gaussian-shaped filters in harmonic space and their width is set by the parameter B: lower values of B correspond to a tighter localisation in harmonic space (fewer multipoles entering into any needlet coefficient), whereas larger values result in wider harmonic bands. We set $B = 1.3$ to have adequate localisation in harmonic space at

[5] https://javicarron.github.io/mtneedlet.

JCAP01(2025)019

intermediate and small angular scales. At low multipoles, with such a choice of the value of B, needlet bands are so narrow that only a few modes would be sampled by each needlet scale. In this case, the estimation of the input needlet covariance in eq. (3.5) would be highly uncertain and thus significantly deviate from a correct ensemble average. This induces a negative empirical correlation of noise and foreground residuals with the CMB signal in the output solution, known as the NILC *bias* [41]. One of the main observable effects of NILC bias is a loss of power, quantified by ${C_\ell}^{\rm bias}$, in the computed output power spectrum, $C_\ell^{\rm out}$, with respect to the sum of contributions from single components:

$$ {C_\ell}^{\rm out} - ({C_\ell}^{\rm CMB} + {C_\ell}^{\rm fg,res} + {C_\ell}^{\rm n,res}) = {C_\ell}^{\rm bias}, \tag{3.7} $$

which is sourced by the negative cross-correlation terms. In eq. (3.7), ${C_\ell}^{\rm CMB}$, ${C_\ell}^{\rm fg,res}$ and ${C_\ell}^{\rm n,res}$ represent angular power spectra of, respectively, the input CMB signal, foregrounds and noise residuals. If ${C_\ell}^{\rm CMB}$ is much larger than $({C_\ell}^{\rm fg,res} + {C_\ell}^{\rm n,res})$, the angular power spectrum of the reconstructed CMB signal would be underestimated and this would impact the final inference of the cosmological parameters. The same effect also arises if the size of the spatial domain over which covariance is computed is too small. In order to overcome the NILC bias due to narrow needlet bands at low multipoles, we merge together the first 15 needlet bands into a unique band as follows:

$$ b_0^{\rm new}(\ell) = \sqrt{\sum_{j=0}^{14} b_j^2(\ell)}. \tag{3.8} $$

The final configuration of harmonic needlet bands is shown in figure 1. We adopt these filters to perform needlet deprojection of input multifrequency B-mode maps and then we linearly combine the needlet maps obtained to get the blackbody solution with lowest variance at each needlet scale.

4 Procedure to set requirements

In this section we summarise the procedure we use to find requirements on the relative polarisation gain calibration. We describe how we compute the bias on the tensor-to-scalar ratio caused by the presence of this systematic effect and how we then set requirements.

4.1 Tensor-to-scalar ratio bias

To estimate the bias on r due to gain mis-calibration, we apply the NILC algorithm on two distinct sets of maps, with the same CMB and noise realisations: one corresponds to the ideal calibration of the relative polarisation gain i.e. $\Delta g_\nu = 0$ for all frequencies (see eq. (2.4)); and the other uses a set of maps where the gain mismatch ($\Delta g_\nu \neq 0$) is injected in a specific frequency channel ν. The component-separation step returns two different CMB solutions, noted as $m_{\rm cmb}(\Delta g_\nu = 0)$ and $m_{\rm cmb}(\Delta g_\nu \neq 0)$. We then apply the *Planck GAL60* Galactic mask,[6] which retains a sky fraction $f_{\rm sky} = 60\%$. For both sets, we compute the B-mode

[6] https://pla.esac.esa.int.

JCAP01(2025)019

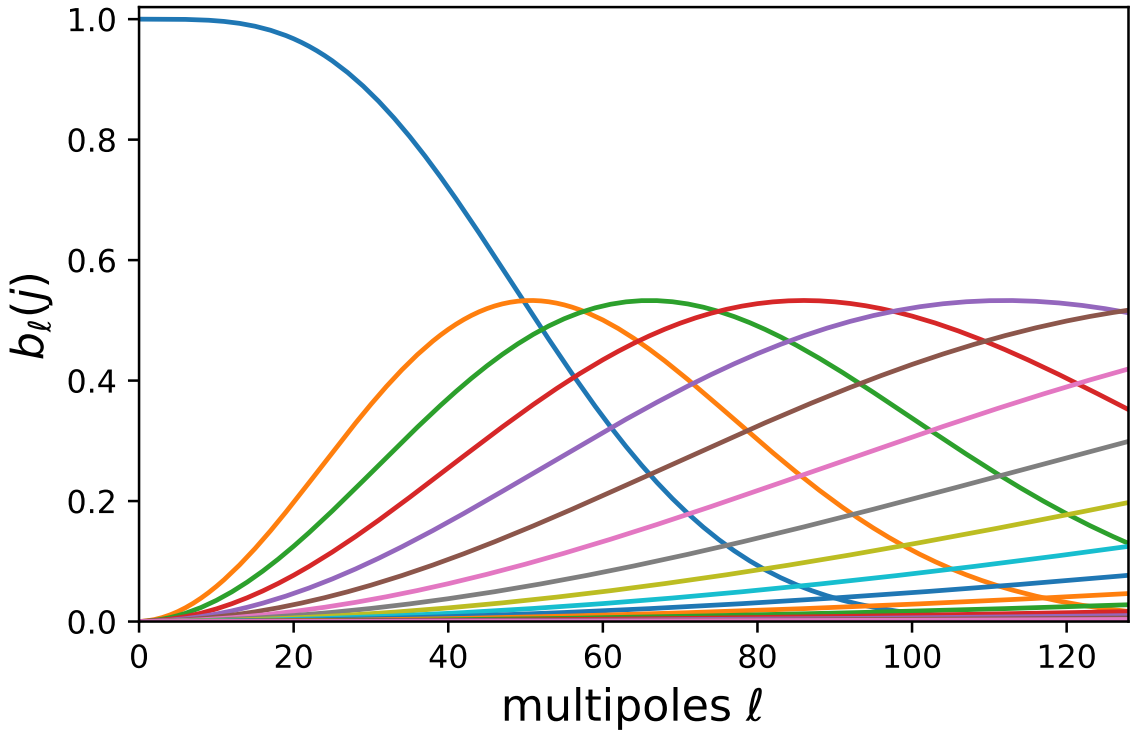

Figure 1. Configuration of Mexican-hat needlet bands adopted in this work. The needlet bands are shown in different colours for each needlet scale j. On the x-axis the multipoles ℓ with $\ell_{\rm max} = 128$, while the y-axis, the needlet filters, $b_j(\ell)$, generated adopting a value of the needlet width parameter $B = 1.3$. The first needlet band features a larger amplitude as it is obtained by merging together multiple bands according to eq. (3.8).

angular power spectrum of the residual maps, derived from the difference between output NILC solutions and input CMB map, thus obtaining

$$\begin{aligned} C_\ell^{\rm res}(\Delta g_\nu = 0) &= C_\ell^{\rm fg,res}(\Delta g_\nu = 0) + C_\ell^{\rm n}(\Delta g_\nu = 0)\,, \\ C_\ell^{\rm res}(\Delta g_\nu \neq 0) &= C_\ell^{\rm fg,res}(\Delta g_\nu \neq 0) + C_\ell^{\rm n}(\Delta g_\nu \neq 0) + C_\ell^{\rm cmb,dist}\,, \end{aligned} \tag{4.1}$$

with $C_\ell^{\rm fg,res}$ and $C_\ell^{\rm n}$, respectively, the foregrounds and instrumental noise contribution after component separation, while $C_\ell^{\rm cmb,dist}$ is a residual term associated with the distortion of the input CMB signal, which deviates from a perfect blackbody due to gain mis-calibration. This contribution is null in the case of an ideal gain calibration $\Delta g_\nu = 0$. We call the BB residual power spectra for the cases with and without mis-calibration, respectively, $C_\ell^{\rm res}(\Delta g_\nu \neq 0)$ and $C_\ell^{\rm res}(\Delta g_\nu = 0)$. The angular power spectra are computed with the `anafast` routine implemented in the `healpy`[7] module [72]. This procedure does not account for correlations among multipoles induced by masking. However, as discussed in ref. [48], this effect proves to have a negligible impact on the assessment of foreground and noise residual power spectra for large sky fractions, as considered in this paper. Moreover, in this case, we do not have to take E–B leakage into account, since power spectra are computed directly on B-mode

[7] https://healpy.readthedocs.io/.

JCAP01(2025)019

maps. To finally assess the impact of gain mis-calibration on the recovered CMB B modes, we infer the tensor-to-scalar ratio r from the output observed angular power spectrum ${C_\ell}^{\rm obs}$, by adopting the following log-likelihood function [73, 74]:

$$-\ln\mathcal{L}({C_\ell}^{\rm obs}|r) = \sum_\ell \frac{2\ell+1}{2} f_{\rm sky}\left[\frac{{C_\ell}^{\rm obs}}{{C_\ell}^{\rm th}(r)} + \ln({C_\ell}^{\rm th}(r)) - \frac{2\ell-1}{2\ell+1}\ln({C_\ell}^{\rm obs})\right], \tag{4.2}$$

where

$${C_\ell}^{\rm obs} = {C_\ell}^{\rm res} + {C_\ell}^{\rm lensing}, \tag{4.3}$$

and the theoretical BB power spectrum ${C_\ell}^{\rm th}$ is given by

$${C_\ell}^{\rm th}(r) = r{C_\ell}^{{\rm GW},r=1} + {C_\ell}^{\rm lensing} + {C_\ell}^{\rm res,eff}. \tag{4.4}$$

In the equations above, $C_\ell^{\rm lensing}$ is the B-mode spectrum induced by gravitational lensing, $C_\ell^{{\rm GW},r=1}$ is the theoretical B-mode power spectrum sourced by tensor perturbations only for $r=1$, while the term $C_\ell^{\rm res,eff}$ corresponds to a template model of noise and foreground residuals after component separation. Such a template power spectrum is obtained by applying NILC on 100 simulations (with different CMB and noise realisations) of *LiteBIRD* B-mode data in the case of ideal gain calibration and averaging over the corresponding $C_\ell^{\rm res}(\Delta g = 0)$.

We evaluate the likelihood function in eq. (4.2) over a grid of values of r in the range $r \in [-1\times10^{-4}, 0.003]$ in steps of $\Delta r = 2\times10^{-7}$. We consider also $r<0$ values in order to allow for negative biases on r (we recall that in all our simulations the CMB component is generated assuming $r=0$). Note that negative values of r do not cause ${C_\ell}^{\rm th}(r)$ to become negative in the logarithm of eq. (4.2) thanks to the presence of ${C_\ell}^{\rm lensing}$ and ${C_\ell}^{\rm res,eff}$ terms, which make the theoretical power spectrum ${C_\ell}^{\rm th}(r)$ always positively defined. We obtain the best-fit values of r as the peak of the likelihood defined in eq. (4.2), for both the mis-calibrated and ideal cases, and assess the bias due to the presence of this systematic effect, δ_r, as

$$\delta_r = r(\Delta g_\nu \neq 0) - r(\Delta g_\nu = 0). \tag{4.5}$$

We note that the inferred value of r is driven by any deviation of an observed residual power spectrum with respect to a model ${C_\ell}^{\rm th}$ (see eq. (4.4)) in which no systematic effect is present. Therefore, the recovered tensor-to-scalar ratio in the ideal calibration case $r(\Delta g_\nu = 0)$ is compatible with zero for each simulation.

4.2 Summary of the procedure

We can now summarise the complete procedure employed to set requirements on the Δg_ν parameter for *LiteBIRD*.

1. We generate the input multi-frequency maps by co-adding the simulated CMB signal, foregrounds and instrumental noise for each *LiteBIRD* frequency channel, as described in section 2.2.

JCAP01(2025)019

2. Using eq. (2.4), we simulate the effect of an imperfect gain calibration at frequency ν by applying a gain calibration factor g_ν drawn from a Gaussian distribution whose standard deviation is given by the Δg_ν parameter. All other frequency maps are therefore left unaltered. At this stage, for each realisation of CMB and noise components, we have two sets of maps: an ideal one with perfect gain calibration $m(\Delta g_\nu = 0)$; and one that includes the systematic effect $m(\Delta g_\nu \neq 0)$.

3. We apply the NILC component-separation procedure to both simulated data sets. This step returns two distinct CMB B-mode solutions in the pixel domain, $m_{\rm cmb}(\Delta g_\nu = 0)$ and $m_{\rm cmb}(\Delta g_\nu \neq 0)$; we then apply a 60% sky cut to mask the Galactic plane.

4. We compute the residual power spectra $C_\ell^{\rm res}(\Delta g_\nu = 0)$ and $C_\ell^{\rm res}(\Delta g_\nu \neq 0)$, as defined in eq. (4.1). Using the likelihood function in eq. (4.2), we derive the best-fit tensor-to-scalar ratio in both cases, $r(\Delta g_\nu = 0)$ and $r(\Delta g_\nu \neq 0)$, and compute the bias δ_r as in eq. (4.5).

5. We repeat the four steps above for different values of Δg_ν. For all Δg_ν values, we consider 100 simulations with different realisations of CMB, noise and g_ν, obtaining therefore 100 values of δ_r.

6. We build the histogram of the bias distribution for each value of Δg_ν and estimate the quantity $\Delta = \sqrt{\mu^2 + \sigma^2}$ of that distribution (see section 5.1) with μ the mean value and σ the standard deviation. The Δ quantity is equivalent to the root mean square (RMS) of the distribution.

7. We derive an empirical relation for Δ as a function of Δg_ν.

8. From this relation, we obtain the requirement on the gain calibration, $\Delta g_{\rm req}$, for each frequency ν. This corresponds to the value of Δg_ν for which Δ is equal to the gain systematic budget allocated to a single channel $\delta_r^{\rm req}$, $\delta_r^{\rm req} = 6.5 \times 10^{-6}/22$,[8] [48].

9. We repeat steps 1 to 8 for all *LiteBIRD* frequency channels and obtain $\Delta g_{\rm req}(\nu)$, which represent the requirements on each single frequency channel.

5 Results

In the following we summarise our results, including the requirements obtained on the single frequency channels (section 5.1) and the impact on the tensor-to-scalar ratio when all frequency channels are mis-calibrated simultaneously (section 5.2). In section 5.1, the systematic effect is propagated through a single frequency channel, considering different amplitudes of the gain calibration uncertainty Δg_ν (eq. (2.4)). The requirement on Δg_ν, being the value for which the single-channel gain systematics budget ($\delta_r^{\rm req} = 6.5 \times 10^{-6}/22$) is met, is then derived for each *LiteBIRD* frequency. In section 5.2, the systematic error is injected into all frequency channels simultaneously, their respective gain calibration factors being

[8] The total budget assigned to the gain systematic effects for *LiteBIRD*, equal to $\Delta r = 6.5 \times 10^{-6}$, is uniformly distributed over all frequency channels. Therefore, the budget associated to a single frequency channel is equal to $\delta_r^{\rm req} = 6.5 \times 10^{-6}/22$.

JCAP01(2025)019

sampled from Gaussian distributions whose widths are set by the requirements per-channel $\Delta g_{\rm req}(\nu)$ derived in section 5.1. By doing so, we assess whether the total budget allocated to gain systematics ($\Delta r = 6.5 \times 10^{-6}$) is fulfilled, considering the previously derived set of requirements. In this analysis, for simplicity, we assume the gain calibration errors to be uncorrelated among the frequency channels. In a more realistic situation these errors are supposed to be partially correlated due to the gain calibration procedure and this is expected to lead to less stringent constraints on the gain calibration. Therefore, the derived set of requirements is considered a conservative one.

5.1 Single frequency requirements

The definition of requirements on the gain calibration accuracy relies on the choice of a unique quantity derived from our δ_r distribution, which should encompass all the statistical variations due to a gain systematic effect. One could look for the value of Δg for which the mean value of δ_r coincides with the assigned budget. However, we observe that for increasing values of Δg, the mean value of δ_r fluctuates around zero. Indeed, gain calibration uncertainties have a negligible impact on average, this being expected because the values of the gain calibration factor g are drawn from a Gaussian distribution centred at one. On the other hand, we clearly note an effect of gain calibration uncertainties on a single simulation, which translates into a larger standard deviation of the distribution, as we strengthen the amplitude of the perturbation (see figure 2). We therefore take as a reference the quantity $\Delta = \sqrt{\mu^2 + \sigma^2}$ derived from the δ_r distribution, this latter taking into account both the *bias* μ (representing the deviation of the δ_r mean value from zero) and the *extra variance* σ. Note that this extra variance is induced by the presence of gain calibration uncertainties only and does not contain contributions from the noise variance and foreground residual uncertainties due to component separation. Indeed, as mentioned in section 4.2, the δ_r distribution is derived from a difference of r in ideal calibration and mis-calibrated cases therefore the contribution to the variance from the noise and foreground residuals cancels out. In our analysis, the contribution from the bias is negligible and we could equivalently use only the standard deviation of the distribution as a reference quantity. Such a statement is not necessarily true for other systematic effects or component-separation techniques, however, and therefore we use the Δ quantity to remain general.

We perturb independently each channel, considering several values of Δg_ν (varying in a common range for all channels) and translate it into Δ variations. From this, we can determine the sensitivity of each channel under gain calibration uncertainties, thus allowing us, for the rest of the analysis, to adapt and tighten the range of Δg_ν values (linearly spaced) for each frequency. Afterwards, we perform the steps 1 to 6 described in section 4.2 and obtain for each *LiteBIRD* frequency channel, a distribution of δ_r for eight different gain calibration uncertainties Δg_ν, varying in different ranges. As an example, figure 2 shows the bias distribution for the LFT 100 GHz channel for three different values of Δg_ν, namely 0.004, 0.007 and 0.01. From each distribution we derive the mean value of the bias, $\mu(\delta_r)$ and the standard deviation $\sigma(\delta_r)$ and compute Δ, for each value of Δg. The amplitude of Δ as a function of the gain calibration uncertainty for each frequency channel is shown in figure 3. As expected, at all frequencies the amplitude of Δ increases with the gain calibration uncertainty.

JCAP01(2025)019

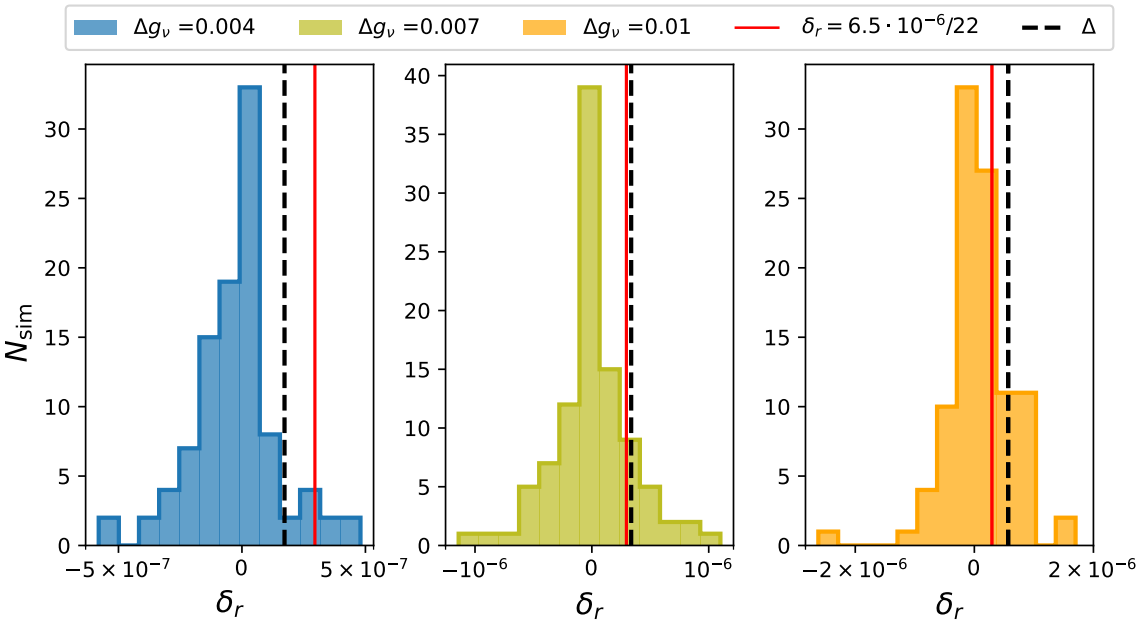

Figure 2. Distribution of δ_r (for 100 different simulations) when the *LiteBIRD* LFT 100 GHz frequency maps are affected by gain calibration uncertainties of $\Delta g_\nu = 0.004$ (left), 0.007 (centre) and 0.01 (right); see eqs. (2.3) and (2.4). The red solid vertical line represents the gain systematic budget per channel ${\delta_r}^{\rm req} = 6.5 \times 10^{-6}/22$, while the dashed black vertical line shows the value of $\Delta = \sqrt{\mu^2 + \sigma^2}$.

We observe that the largest values of Δ are obtained for the central frequency channels, which correspond to those having larger NILC weights. Indeed, for small values of Δg ($\lesssim 4 \times 10^{-2}$) the assigned budget is exceeded at CMB frequencies (from LFT-119 to MFT-195), while the low and high-frequency channels are less senstive and allow larger amplitudes of the gain perturbation. This trend is opposite to that found in ref. [52] and highlights the different impact of gain mis-calibration when considering different component-separation approaches.

Once the Δ values as a function of Δg_ν are obtained for each channel, we perform an interpolation in order to obtain an empirical relation among these two quantities. This is well approximated by a linear function for all frequency channels. These interpolating functions are then employed to derive the requirement on the gain calibration for each *LiteBIRD* frequency channel as the value of Δg_ν for which $\Delta = \delta_r^{\rm req} = 6.5 \times 10^{-6}/22$, the budget allocated to a single frequency channel. The latter is derived by uniformly distributing *LiteBIRD*'s total gain systematic budget ($\Delta r = 6.5 \times 10^{-6}$) over the 22 distinct frequency channels. As an example, we show in figure 4 the amplitude of Δ as a function of Δg_ν for the LFT 100 GHz channel, together with the corresponding interpolating function. The intercept with the horizontal line $\delta_r^{\rm req}$ allows us to determine $\Delta g_{\rm req}$.

We report the derived requirements per channel $\Delta g_{\rm req}(\nu)$ in table 2. We find that the requirements on Δg_ν range between 0.16 and 3.22%. Such values are less restrictive (by two orders of magnitude) than those obtained when the `FGBuster` parametric component-separation pipeline is applied to an analogous simulated *LiteBIRD* data set, as found in ref. [52]. We recall that NILC, and blind methods more generally, construct a linear combination of

JCAP01(2025)019

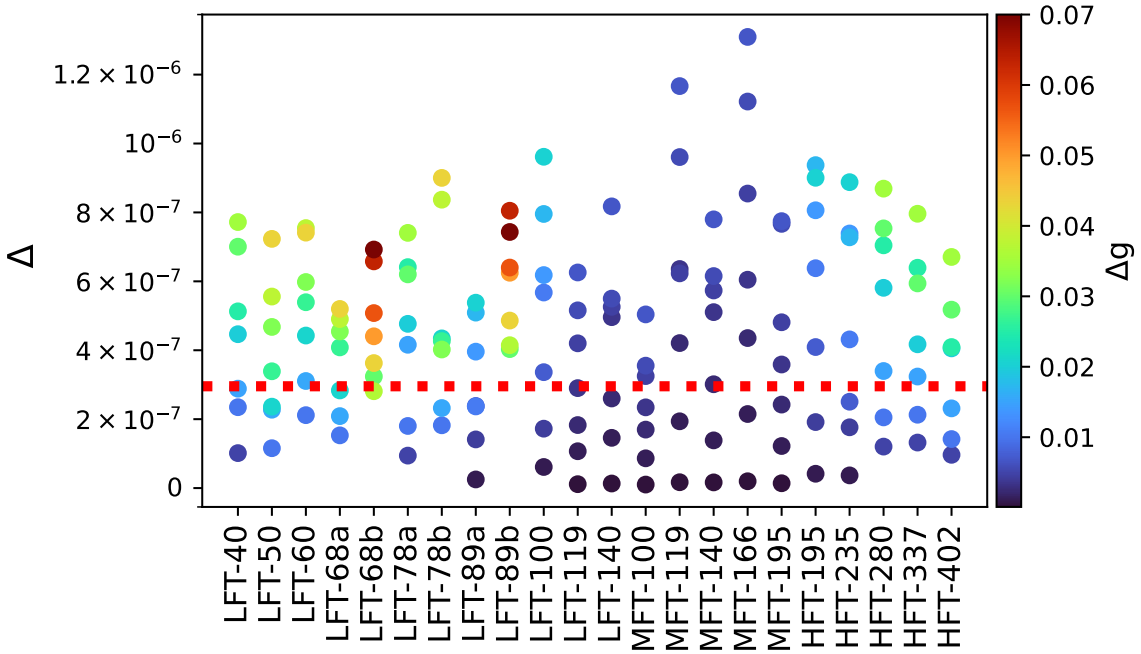

Figure 3. Evolution of Δ ($= \sqrt{\mu^2 + \sigma^2}$) as a function of the gain calibration uncertainty Δg_ν for all *LiteBIRD*'s channels. The red dashed horizontal line corresponds to the gain systematic budget per channel ${\delta_r}^{\rm req} = 6.5.10^{-6}/22$.

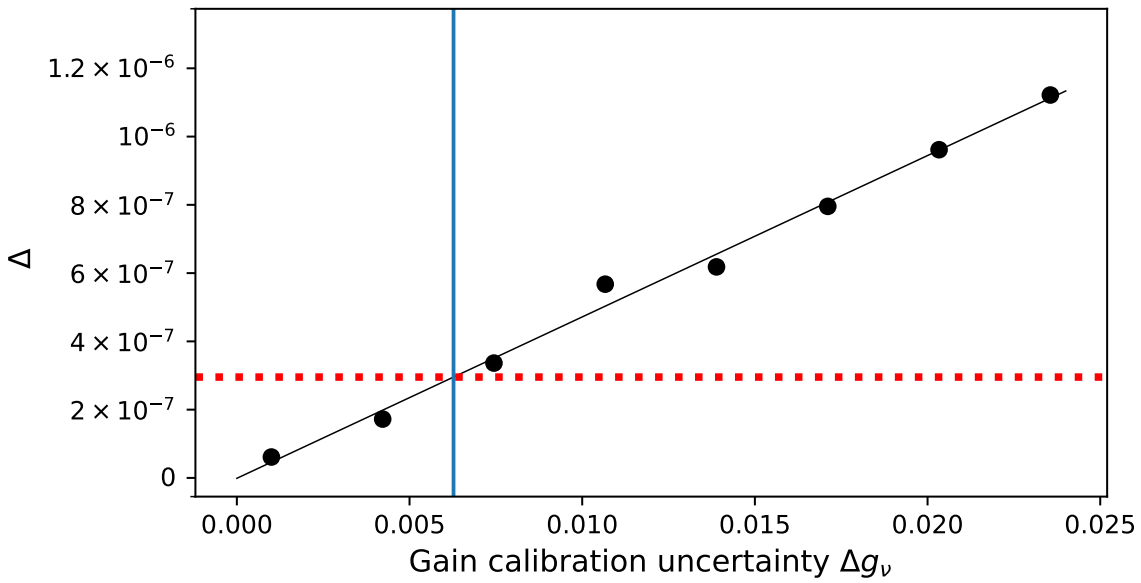

Figure 4. Variation of Δ ($= \sqrt{\mu^2 + \sigma^2}$) with the gain calibration uncertainty Δg_ν for the LFT 100 GHz channel. The red dashed line shows the single channel gain systematic budget ${\delta_r}^{\rm req} = 6.5 \times 10^{-6}/22$ and the blue solid line corresponds to the requirement on the gain calibration accuracy obtained for the LFT 100 GHz channel, namely 0.63%.

JCAP01(2025)019

Channel Label	Single channel $\Delta g_{\rm req}(\nu)$[%]
LFT-40	1.36
LFT-50	2.19
LFT-60	1.51
LFT-68a	2.12
LFT-68b	3.22
LFT-78a	1.27
LFT-78b	1.72
LFT-89a	1.04
LFT-89b	2.05
LFT-100	0.63
LFT-119	0.33
LFT-140	0.25
MFT-100	0.43
MFT-119	0.17
MFT-140	0.23
MFT-166	0.16
MFT-195	0.26
HFT-195	0.52
HFT-235	0.70
HFT-280	1.18
HFT-337	1.31
HFT-402	1.70

Table 2. Requirements on the relative polarisation gain calibration for all *LiteBIRD* frequency channels. This set of requirements is obtained assuming the `d0s0` sky model.

frequency maps in order to recover th CMB blackbody signal. It follows that the weights of the linear combination are larger at frequencies where the CMB is less obscured by other sources of emission, and they tend to be smaller at frequencies where foregrounds are more dominant. Therefore, gain calibration uncertainties have a larger impact in the frequency range where NILC weights are larger, thus leading to more stringent requirements around CMB frequencies. We then expect a correlation between NILC weights and the channels sensitivity to gain calibration uncertainties, quantified in terms of the requirement on Δg_ν.

In figure 5, we show the inverse of the requirements, $\Delta g_{\rm req}^{-1}(\nu)$, and the average NILC weights in the first needlet band ($\bar{\omega}_\nu^0$), as a function of the frequency. We can see that the frequency dependence of $\Delta g_{\rm req}^{-1}(\nu)$ is strongly correlated with that of $\bar{\omega}_\nu^0$. We report the correlation with the NILC weights in the first needlet band $j = 0$, since this band is the one that samples modes at the largest angular scales and has more constraining power on r. We observe correlations also for the other needlet scales. The trend observed in figure 5 also explains that for the channels observing at the same frequency but with different sensitivities,

JCAP01(2025)019

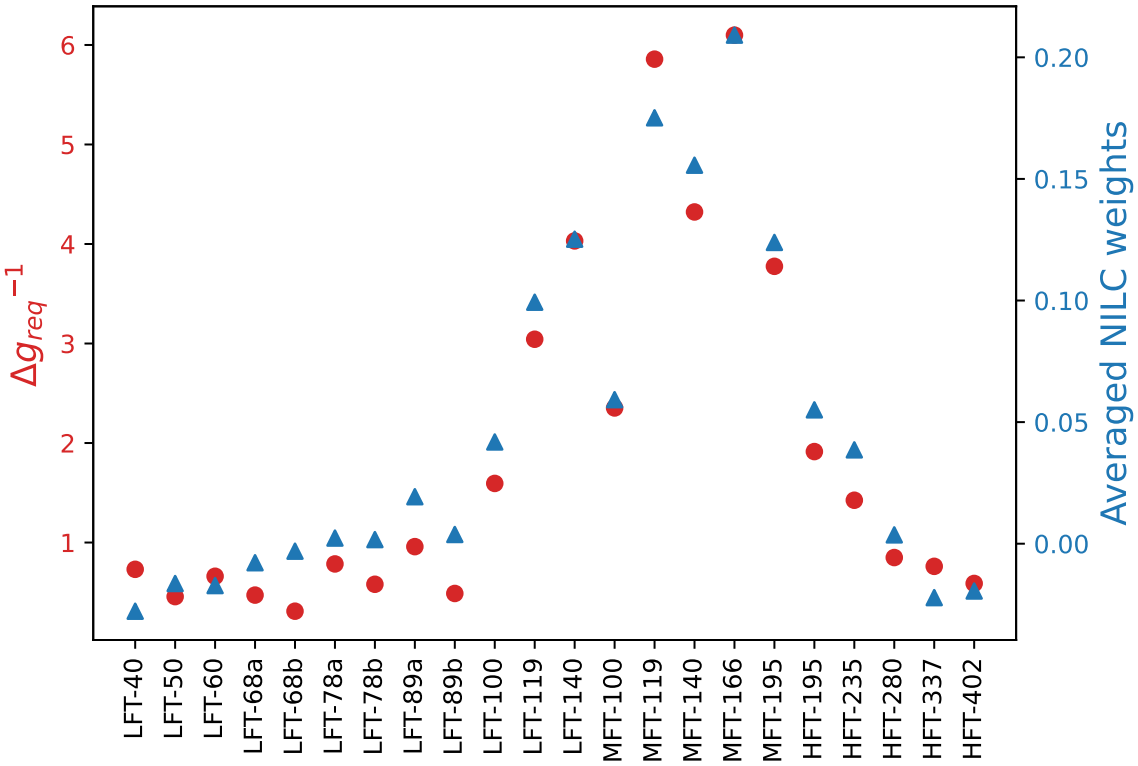

Figure 5. Trend of the inverse of the requirements on the relative polarisation gain calibration $\Delta g_{\rm req}^{-1}$ (red points), reported in table 2, and averaged NILC weights in the first needlet band $\bar{\omega}_\nu^0$ (blue triangles) for the different *LiteBIRD* frequency channels.

we observe more stringent requirements for the a-channels than for the b-channels. The b-channels possessing a higher noise level, tend to be down-weighted (with respect to a-channels) in the NILC process, and therefore are less sensitive to gain calibration uncertainties.

5.2 Simultaneous mis-calibration of all channels

After obtaining requirements separately for each frequency channel, we assess whether the impact on the tensor-to-scalar ratio is compatible with the total budget allocated to gain calibration uncertainties when all frequency channels are mis-calibrated assuming the $\Delta g_{\rm req}(\nu)$ values reported in table 2. Each frequency channel is affected by a specific gain calibration factor derived from a Gaussian distribution whose standard deviation corresponds to the requirements $\Delta g_{\rm req}(\nu)$ shown in table 2.

We run the NILC component-separation process on a set of 500 map realisations, and, for each of them, we determine δ_r value as the difference between the tensor-to-scalar ratio r for the perturbed and unperturbed case (see eq. (4.5)). The distribution of δ_r among all 500 realisations is shown in figure 6. The resulting value of $\Delta \approx 1.29 \times 10^{-6}$ is lower than the *LiteBIRD* gain systematics budget $\Delta r = 6.5 \times 10^{-6}$ [48] by a factor of approximately 5. This result shows that the biases on the tensor-to-scalar ratio δ_r originating from separately mis-calibrating all frequency channels by their corresponding $\Delta g_{\rm req}(\nu)$, do not add up linearly if the same mismatches are applied simultaneously to all channels.

JCAP01(2025)019

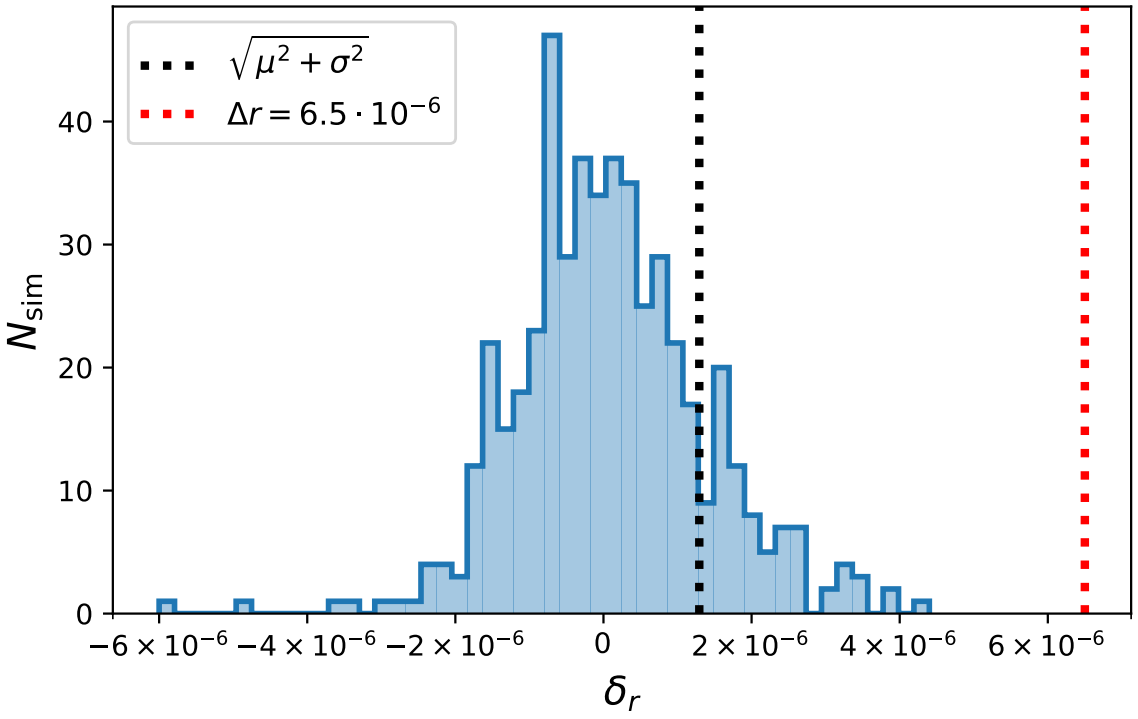

Figure 6. Distribution of δ_r for $N_{\rm sim} = 500$ when all channels are perturbed simultaneously with their corresponding requirement $\Delta g_{\rm req}(\nu)$ (reported in table 2). The dotted red line indicates the budget allocated to gain systematics $\Delta r = 6.5 \times 10^{-6}$ and the dotted black line represents the value of $\Delta = \sqrt{\mu^2 + \sigma^2}$ of the distribution.

This result originates from the adaptive behaviour of the NILC weights, which automatically tend to readjust themselves to the different frequency scalings of the sky components. Such re-adjustment of the weights induces correlations in the impact of mis-calibration of different channels, which does not allow a linear addition of the contributions from single channel mismatches. Figure 6 shows that a considerable margin is available before reaching the threshold bias allocated to gain mis-calibration, suggesting that such requirements may be revisited, e.g. by relaxing the most stringent ones and reducing those for less sensitive channels. Another possibility is to apply a common multiplicative factor, α_g, to the set of requirements presented in table 2 and simultaneously mis-calibrate all channels by these rescaled $\Delta g'_{\rm req}(\nu) = \alpha_g \Delta g_{\rm req}(\nu)$ values. To do this, we consider multiple values of α_g in the range $[1, 6]$. We then interpolate the evolution of Δ derived from the δ_r distributions as a function of α_g, and estimate the α_g value that leads to a total bias of $\Delta r = 6.5 \times 10^{-6}$. Figure 7 indicates that the Δ dependence on α_g is quadratic. Such a trend is explained by the fact that, since we apply a common scaling factor to all channels simultaneously, the amplitude of output residuals is expected to scale linearly with α_g and therefore the output BB power spectrum will be proportional to ${\alpha_g}^2$.

Using the interpolating function shown in figure 7, we find that the total gain systematics budget is reached for $\alpha_g \approx 4.4$. We are therefore able to set an upper limit on the relative polarisation gain requirements, corresponding to an amplification by this factor of the $\Delta g_{\rm req}(\nu)$

JCAP01(2025)019

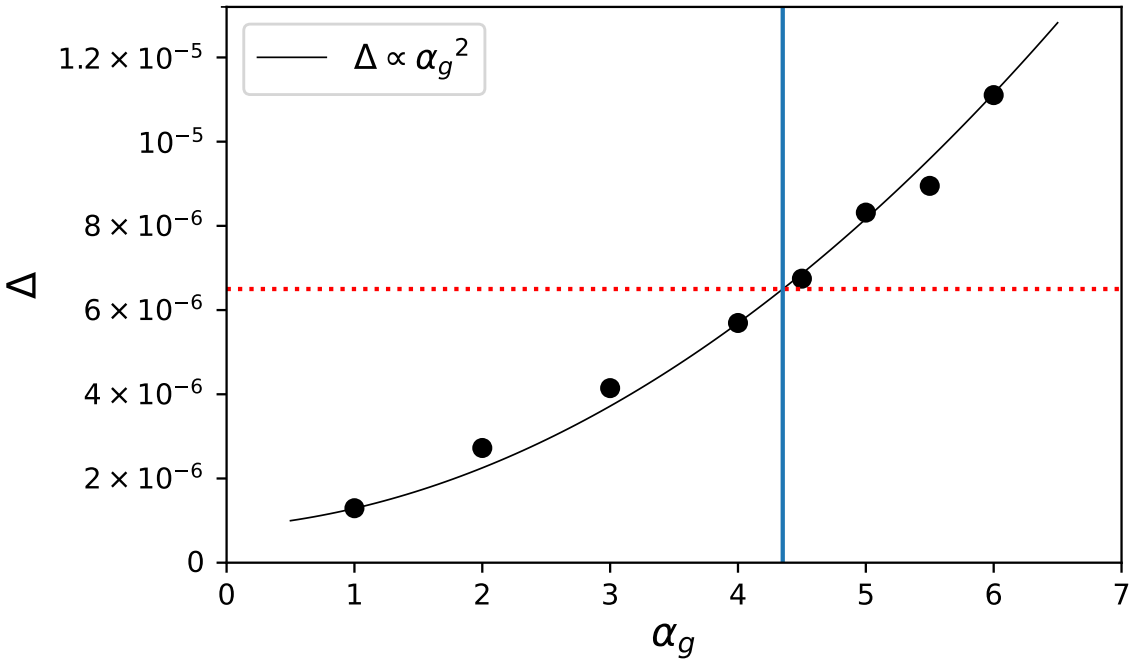

Figure 7. The quantity $\Delta = \sqrt{\mu^2 + \sigma^2}$ as a function of α_g. The red dotted line shows the total gain systematics budget $\Delta r = 6.5 \times 10^{-6}$, while the blue solid line corresponds to the value of α_g by which the requirements on `d0s0` should be rescaled to match the total gain systematics budget.

values reported in table 2. Overall, the available margin between the obtained Δ and threshold values could possibly absorb larger impacts of gain calibration uncertainties in scenarios with more complex foregrounds, as shown in the next section.

5.2.1 Extension to more complex sky models

We now turn to investigating the impact on δ_r if the requirements presented in table 2 are applied simultaneously to frequency maps, but assuming more complex foreground models.

1. Sky model. Recall that the results presented in section 5.2 are obtained considering a sky model with constant synchrotron and dust spectral indices across the sky (`d0s0` model) and using NILC component separation. The `s0` and `d0` models are, however, a simplification of the actual Galactic emission and constitute the lowest level of complexity in the foreground modelling provided by the `PySM` package.

The first option would be to set requirements on the gain calibration following the procedure presented in section 4.2 for more complex sky models, these being as realistic as possible in order to mimic the conditions of real polarisation observations. This would, however, need an extremely accurate knowledge of the Galactic foreground spectral energy distribution. Such knowledge has not yet been achieved but investigating it is generating much interest in the CMB community [39, 75, 76].

In this section, we aim to assess if the requirements derived for the `d0s0` foreground model are robust against more complex foreground scenarios. We thus consider two additional `PySM`

JCAP01(2025)019

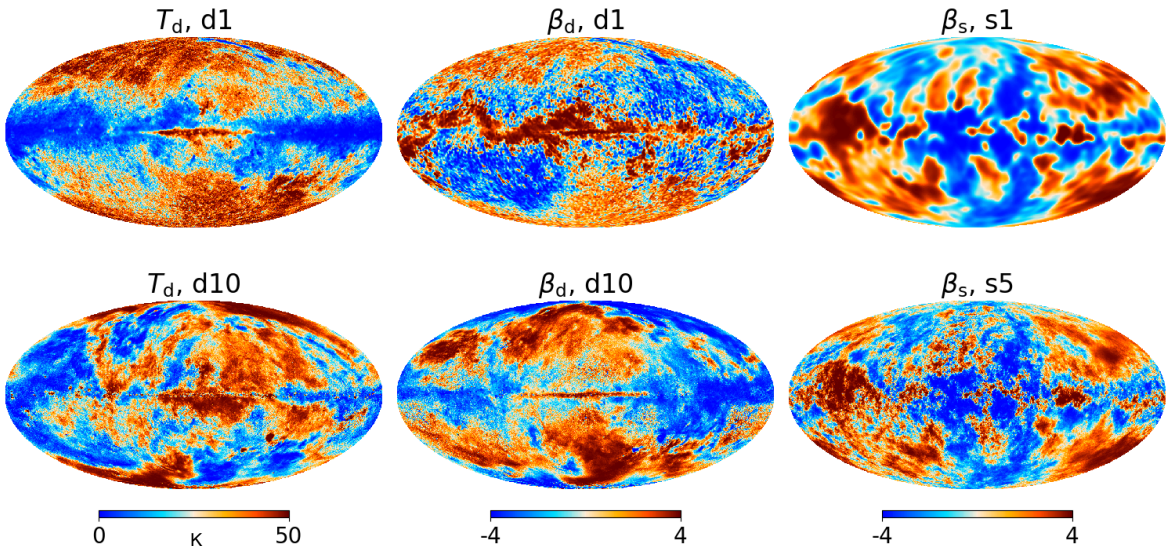

Figure 8. Polarised dust and synchrotron spectral indices β_d, T_d and β_s for `d1s1` (top) and `d10s5` (bottom) sky models. These maps are generated for a resolution parameter of $N_{side} = 512$.

sky models: `d1s1` and `d10s5`. In the `d1s1` model, the dust and synchrotron spectral indices vary across the sky. The dust template corresponds to the 353 GHz map from *Planck* [5, 31] and the dust spectral parameters maps are obtained by applying the `Commander` pipeline [34] to the *Planck* data set. The synchrotron template corresponds to the *WMAP* 9-year 23 GHz Q/U maps [3] and the spectral index map is obtained by combining the *Haslam* 408-MHz data and *WMAP* 23 GHz 7-year data [60]. In the `d10s5` model, the synchrotron spectral index map is rescaled to account for the larger variability observed by the S-PASS experiment [62], which mapped synchrotron emission at 2.3 GHz. The maps of thermal dust spectral parameters are obtained by applying the GNILC component-separation technique to the *Planck* data set. The variations of polarised dust and synchrotron spectral indices T_d, β_d and β_s across the sky are shown in figure 8 for both sky models described above.

2. MC-NILC component separation. In a framework with complex foreground emission, the NILC pipeline, which performs simple local variance minimisation across the sky, may be suboptimal, since it is not enginereed to fully handle the local spectral variations of foregrounds. We therefore use the MC-NILC (Multi-Clustering Needlet ILC) [45] foreground-cleaning method which aims at minimising the variance within sky patches, also called *clusters*. MC-NILC accounts for the spatial variability of spectral properties of foreground B modes by identifying a tracer of their distribution across the sky, with a limited number of a priori assumptions. The spectral distribution of dust and synchrotron spectral parameters are assessed by computing the ratio of foreground B-mode maps at two distinct frequencies: one at high frequency (337 GHz) and one at CMB frequencies (119 GHz). Such a ratio allows us both to estimate an effective thermal dust spectral index and an emission ratio of synchrotron and dust at the CMB-dominated frequency.

In this analysis, we consider two distinct approaches of MC-NILC. Firstly, the *ideal* approach where clusters are built for each needlet scale from the ratio of the input 337 GHz

JCAP01(2025)019

and 119 GHz foreground-only B modes (noiseless). Note that the ideal MC-NILC approach is not data-driven because the foreground B-mode templates are directly derived from simulations. However, such an approach remains helpful to assess the maximal capability of MC-NILC to perform foreground subtraction, since the ratio of simulated foreground B modes is able to trace, in an optimal way, the spatial variations of spectral indices across the sky. In the context of gain calibration, the ideal MC-NILC allows us to derive the impact of gain calibration uncertainties on more complex foreground modelling when the employed component-separation method is optimal. Secondly, we consider *realistic* MC-NILC, where templates of foreground B modes at the two frequencies of interest (for the construction of the tracer) are obtained by applying the Generalised Needlet ILC (GNILC) [43] formalism to observed multi-frequency data. The patches are then built from a unique emission ratio at 337 and 119 GHz of foreground B modes, for all needlet scales. The realistic MC-NILC has the benefit of being able to build a tracer of the spectral variations of foregrounds directly from observed multi-frequency data. However, it suffers from residual contamination of CMB and noise in the GNILC foreground templates and therefore the reconstruction of the CMB signal in the end is not as optimal as in the ideal MCNILC approach.

In this study, we consider 50 clusters of equal area, the optimal number of clusters being assessed by comparing the foreground residuals and the bias in the CMB reconstruction after performing MC-NILC on the *LiteBIRD* data set with different numbers of clusters. A detailed description of the sky-patch optimisation is presented in ref. [45]. The variance minimisation is then performed within each cluster using the NILC component separation, considering the same configuration as the one presented in section 3.2.

3. Simulations and results. We simulate multi-frequency maps of CMB, dust, synchrotron and noise, as described in section 2, considering the two different foreground modelling schemes presented above. We propagate the gain calibration uncertainties to all channels simultaneously, according to the requirements in table 2 and apply MC-NILC to a set of 500 realisations. Since we aim to assess the impact of the gain mis-calibration on each simulation, we also apply MC-NILC to the twin set of maps without systematic effects.

We apply a common mask to the output CMB maps, corresponding to the previously used `GAL60` *Planck* mask with an additional 10% obtained by thresholding the averaged foreground residuals map (over 500 simulations, without gain mismatch) smoothed with a FWHM $= 3^\circ$ Gaussian beam. An analogous masking strategy is employed in ref. [48], and retains a 50% fraction of the sky. Note that such a masking strategy cannot be employed to analyse real data because it requires a foreground residuals template not directly accessible from observations. However, as shown in ref. [45], very similar results are obtained with a fully data-driven approach where a template of foreground residuals is derived by combining the MC-NILC weights with the GNILC frequency maps.

For each simulation, the value of δ_r is obtained from the difference between the tensor-to-scalar ratio for the perturbed $r(\Delta g \neq 0)$ and unperturbed cases $r(\Delta g = 0)$ from eq. (4.5), derived using the cosmological likelihood (eq. (4.2)) and considering the power spectrum of respective residuals (eq. (4.1)). The distributions of δ_r for the different sky models when the ideal MC-NILC formalism is employed are shown in figure 9.

JCAP01(2025)019

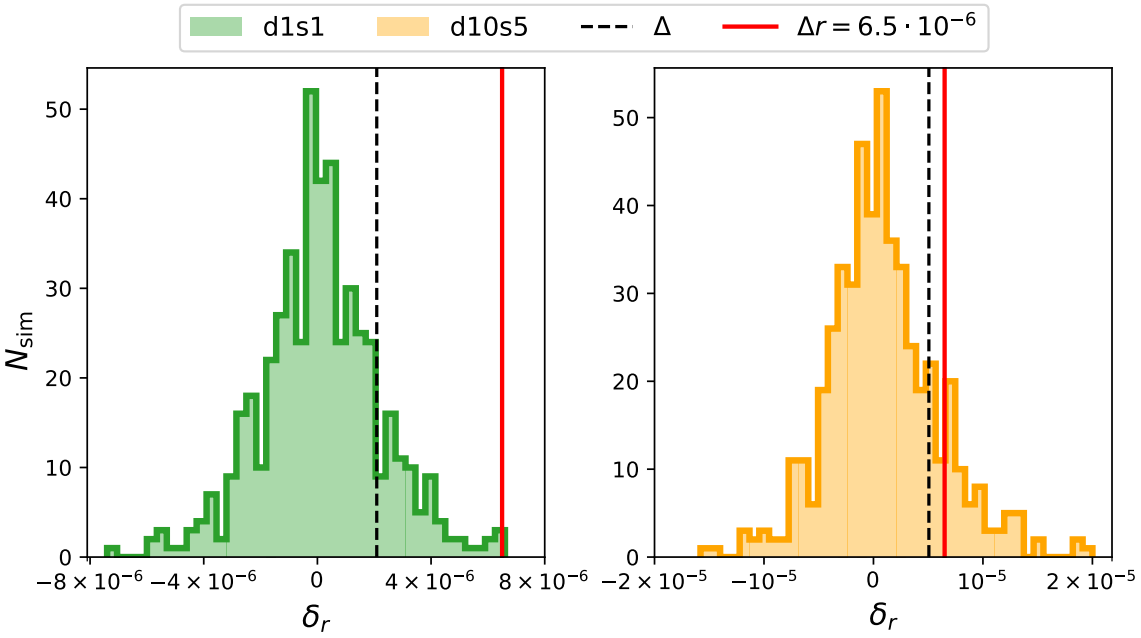

Figure 9. Distribution of δr for 500 simulations when all channels are perturbed simultaneously with their corresponding requirements $\Delta g_{\rm req}(\nu)$. The green histogram represents the distribution of δr when the ideal MC-NILC pipeline is applied on the *LiteBIRD* data set with the `d1s1` sky model while the yellow one corresponds to the `d10s5` case. The red solid line represents the budget allocated to gain systematics $\Delta r = 6.5 \times 10^{-6}$ and the dashed black lines show the value of $\Delta = \sqrt{\mu^2 + \sigma^2}$.

Figure 9 shows that if the ideal MC-NILC component-separation technique is applied on `d1s1` data (left panel), Δ is lower than the total gain systematics budget by a factor of 3. Such a margin is expected, since the ideal version of MC-NILC is able to perform foreground subtraction on the `d1s1` sky almost as efficiently as the baseline NILC in a case with isotropic spectral parameters of the foregrounds. However, the slightly larger contamination by residuals in the MC-NILC `d1s1` case leads to a reduction of the margin with respect to that found in figure 6 with NILC and the `d0s0` model. When ideal MC-NILC is applied to the `d10s5` data set, the obtained Δ value is still below the budget, but larger than in the `d0s0` and `d1s1` cases. This is due to the higher complexity of the sky model, which leads to larger residuals in the CMB reconstruction. This observed trend of Δ highlights that the impact of gain calibration uncertainties on the estimation of the tensor-to-scalar ratio depends on the overall amplitude of residuals and therefore on the effectiveness of the foreground-cleaning step.

In a realistic framework, one way of mitigating the effect of component-separation uncertainties is to marginalise over the foreground residuals. For complex sky models and realistic MC-NILC component separation, the recovered best-fit value of the tensor-to-scalar ratio (without systematics) may indeed no longer be compatible with zero. The aim of such a marginalisation is therefore to reduce as much as possible the foreground residual bias after component separation. Therefore, in the cases where realistic MC-NILC is applied, we perform a marginalisation over foreground residuals to mimic the procedure of a realistic estimate of the tensor-to-scalar ratio for *LiteBIRD*. Starting from the cosmological likelihood

JCAP01(2025)019

given by eq. (4.2), we re-define the theoretical BB power spectrum as

$$C_\ell^{\rm th} = rC_\ell^{\rm GW,r=1} + C_\ell^{\rm lensing} + C_\ell^{\rm n} + \gamma C_\ell^{\rm fg,res}. \tag{5.1}$$

Again, the $C_\ell^{\rm fg,res}$ and $C_\ell^{\rm n}$ quantities correspond to a template of foregrounds and noise residuals, respectively, after component separation, obtained from averaging the MC-NILC noise and foreground residuals over 100 simulations, without systematic effects. In this analysis, the employed foreground-residual template is not obtained through a fully realistic approach, but constructed by combining the weights with the input foreground frequency maps. However, we observe that performing the marginalisation using a foreground-residual template derived through a realistic and fully data-driven approach leads to very similar constraints (3% difference of Δ between both cases, in the `d10s5` configuration). Such a result is in agreement which what has been found in recent studies on primordial B-mode reconstruction from *LiteBIRD*. For this reason, we do not detail the results obtained when considering a realistic foreground residuals template and present only those coming from the ideal scenario. With the expression of the theoretical B-mode power spectrum given by eq. (5.1), the full posterior is now 2-dimensional and defined for r and γ variables, with γ representing the marginalisation factor:

$$-\ln \mathcal{L}(C_\ell^{\rm obs}|r,\gamma) = \sum_\ell \frac{2\ell+1}{2} f_{\rm sky}\left[\frac{C_\ell^{\rm obs}}{C_\ell^{\rm th}(r,\gamma)} + \ln(C_\ell^{\rm th}(r,\gamma)) - \frac{2\ell-1}{2\ell+1}\ln(C_\ell^{\rm obs})\right]. \tag{5.2}$$

From the 2D log-likelihood defined in eq. (5.2), we build the likelihood on r by marginalising over γ values:

$$\mathcal{L}(r) = \frac{\int \mathcal{L}(r,\gamma)d\gamma}{\int \mathcal{L}(r,\gamma)d\gamma dr}. \tag{5.3}$$

Finally, as described in section 4.1, the best-fit value of the tensor-to-scalar ratio corresponds to the peak of the r posterior distribution of eq. (5.3). Thereafter, we perform the marginalisation on the cases for which r (without systematic effects) is not fully compatible with zero i.e. when the realistic MC-NILC pipeline is applied to *LiteBIRD* data sets simulated assuming the `d1s1` and `d10s5` sky models.

In practice, we retrieve the observed BB residual power spectra obtained by applying the realistic MC-NILC pipeline on both `d1s1` and `d10s5` data, in the case of ideal and imperfect gain calibration. Both for ideal and mis-calibrated cases, we apply the 2D likelihood shown in eq. (5.2) on the observed BB power spectra. We consider values of γ in the range $[0, 3]$ with a step size of 0.1, while r varies in the range $[-1\times10^{-4}, 0.003]$ with a 2×10^{-7} step size. Figure 10 represents the 2D-likelihood given by eq. (5.2) in the γ–r plane with $C_\ell^{\rm obs}$ (eq. (4.3)) being the average among 500 simulated BB power spectra. The (γ, r) pair that maximises the 2D-likelihood is $(1, 0)$, thus demonstrating that we have an unbiased estimate of r. The peak value $\gamma = 1$ is expected since the foreground-residual template we are marginalising over corresponds to an average among 500 simulations and this same term appears also in the observed BB power spectrum. Furthermore, we observe that r and γ are only weakly correlated. From the 2D posterior, we then estimate the value of r maximising the

JCAP01(2025)019

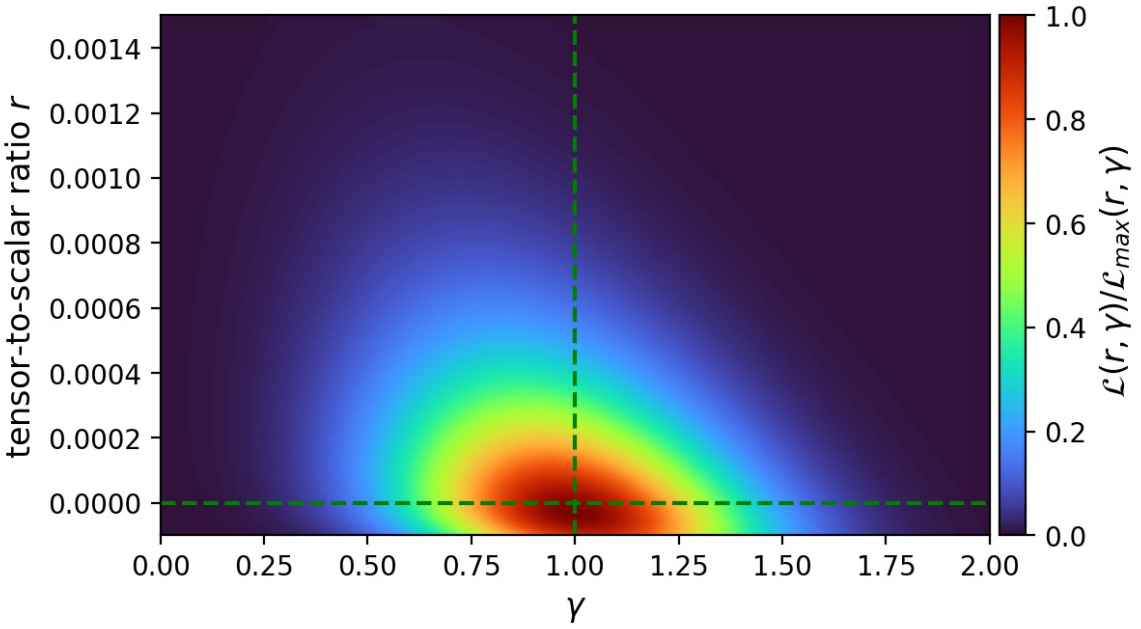

Figure 10. Representation of the 2D likelihood $\mathcal{L}(r, \gamma)$ in the $\gamma - r$ plane. For visualisation purposes, we only display values of r in the range $[-1 \times 10^{-4}, 0.0015]$ and γ in $[0, 2]$. The green dashed line shows the (γ, r) pair maximising $\mathcal{L}(r, \gamma)$.

r likelihood thanks to eq. (5.3), for both calibration cases $r^{\rm marg}(\Delta g = 0)$ and $r^{\rm marg}(\Delta g \neq 0)$, after marginalisation. Finally, we build the δr distribution by differencing $r^{\rm marg}(\Delta g = 0)$ and $r^{\rm marg}(\Delta g \neq 0)$, and compare for each sky model the value of Δ with $\Delta r = 6.5 \times 10^{-6}$.

Figure 11 shows the distribution of δr when we apply the realistic MC-NILC pipeline to our simulations. The value of Δ obtained for `d1s1` sky model is 1.25 times smaller than the budget while for the `d10s5` sky model Δ exceeds the threshold by a factor of approximately 2. Since this last case is the only one where we exceed the allocated budget, we now assess by what factor, denoted ${\alpha_g}^{\rm s5,d10}$, we should reduce the requirements presented in table 2 to match the total gain systematics budget. As done in section 5.2, we interpolate the trend of Δ as a function of ${\alpha_g}^{\rm s5,d10}$ and find the value of the factor for which Δ matches with $\Delta r = 6.5 \times 10^{-6}$. We find that the initial requirements need to be reduced by a factor ${\alpha_g}^{\rm s5,d10} \approx 1.8$ to fulfill the budget, in the case of the `d10s5` sky model with the realistic version of MC-NILC (after marginalisation).

The results presented in section 5.2.1 highlight a clear dependence of the impact of gain calibration uncertainties on the assumed sky model. Indeed, we find that by adopting the same component-separation method (i.e. realistic MC-NILC), the effect induced by gain calibration uncertainties on the tensor-to-scalar ratio estimation is more significant for the `d10s5` case than for `d1s1`, with the former requiring a rescaling of the requirements derived with NILC and the `d0s0` sky model. Given our current ignorance of the true sky model and on the unpredictability of future refinements of the component-separation pipelines, it is not trivial yet to set definitive requirements without assuming a specific sky model and foreground-cleaning technique. We therefore propose a range of requirements whose limits

JCAP01(2025)019

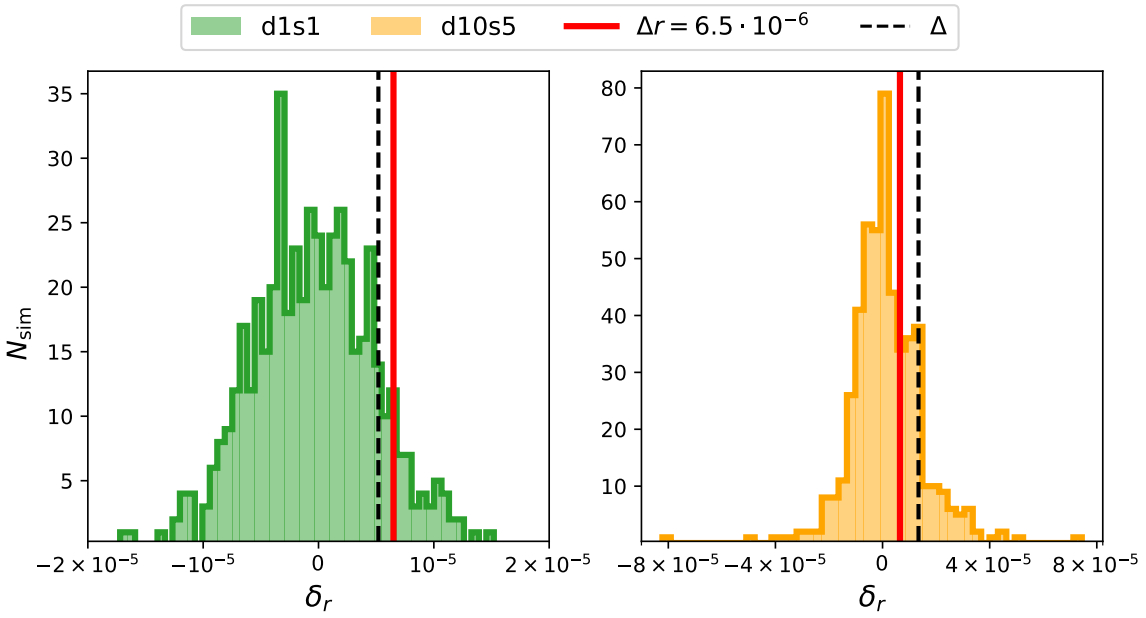

Figure 11. Distribution of δr for 500 simulations when all channels are perturbed simultaneously with their corresponding requirements $\Delta g_{\rm req}(\nu)$ when the realistic MC-NILC pipeline is applied on `d1s1` (left) and `d10s5` (right) *LiteBIRD* simulations. The black dashed lines represent the value of $\Delta = \sqrt{\mu^2 + \sigma^2}$ of each distribution and the red solid line shows the budget allocated to gain systematics, $\Delta r = 6.5 \times 10^{-6}$.

correspond to the most optimistic and pessimistic scenarios presented in this paper. The lower bound is given by the set of requirements derived assuming the `d0s0` sky model with NILC (see table 2), while the upper bound corresponds to the set of requirements rescaled by a factor of 1.8, as needed to meet the allocated budget in the frame of the `d10s5` model with realistic MC-NILC as the component-separation method (including marginalisation).

6 Conclusions

The space-borne mission *LiteBIRD* will target a detection of the primordial tensor perturbations with an overall sensitivity of $\sigma_r \lesssim 10^{-3}$. This requires an exquisite calibration accuracy to mitigate the impact of systematic effects, which otherwise would bias the measurement of r.

In this paper, we have presented a methodology that allows us to derive the requirements on the calibration accuracy of the relative polarisation gain, considering the application of a component-separation pipeline to reconstruct the CMB polarisation B-mode signal in the presence of Galactic foreground emission. Although the presented methodology is general and could be used with any component-separation technique, in our work we have made use of the NILC foreground-cleaning technique (section 3). Unlike for parametric component-separation approaches, NILC performs a reconstruction of the CMB signal without any assumption on the Galactic foreground SED, thus representing a robust technique for any effective model of Galactic emission.

With our procedure, we first set requirements on the gain calibration accuracy needed in each frequency channel of *LiteBIRD*. We did so by simulating the mis-calibration of a single

JCAP01(2025)019

frequency map, applying a homogeneous and constant gain calibration factor g_ν drawn from a Gaussian distribution centred at 1 with standard deviation Δg_ν, while all other channels were left unperturbed. We then derived the bias on r, by computing the difference δ_r between the estimated r for an ideal calibration (i.e. $g_\nu = 1$) and in the case of an imperfect calibration. We applied a cosmological likelihood on the residual B-mode angular power spectra after component separation (see eqs. (4.1) and (4.2)). For each frequency, we considered different values of Δg_ν and determined the empirical relationship between Δg_ν and the quantity $\Delta = \sqrt{\mu^2 + \sigma^2}$, with μ and σ being the mean and standard deviation of the distribution of the bias on the tensor-to-scalar ratio δ_r. This allowed us to estimate the requirement $\Delta g_{\rm req}$ as the value for which we find $\Delta = {\delta_r}^{\rm req} = 6.5 \times 10^{-6}/22$ (section 4.2).

We emphasise that a similar methodology has been applied in the past to obtain requirements for *LiteBIRD*, adopting a parametric component-separation pipeline to recover the CMB signal [52]. In section 5.1, we showed that the requirements on the relative polarisation gain obtained with NILC are less constraining compared to those obtained through the parametric approach [52]. Specifically, as shown in table 2, we found that the frequency channels that are more impacted by the presence of gain calibration uncertainties are located around the minimum of foreground emission (119, 140, and 166 GHz), while in ref. [52] the most sensitive channels appear to be at low and high frequencies, where diffuse Galactic emission is dominant, and thus their mis-calibration largely affects the fit of foreground SEDs. In the case of NILC, indeed the requirements are anti-correlated with the weights (larger for central frequencies) and therefore the channels contributing the most in the CMB reconstruction are those most affected by gain calibration uncertainties. The interpretation of these results relies on the different approaches to foreground cleaning. While NILC absorbs the perturbation in a re-adjustment of weights into the minimum variance combination of channels, the parametric fitting requires a dedicated parametrisation to marginalise over the corresponding unknowns, in order to lower the impact of the systematic effect. In the absence of marginalisation, parametric methods, which assume a well-defined spectral dependence, can produce strongly biased CMB reconstructions.

We also simulated the mis-calibration of all channels at once, using the corresponding channel requirements. In this case, we found a Δ value lower than the total gain systematic budget by a factor of approximately 5. Considering the available margin, we rescale the requirements at all frequency channels by a common factor α_g: $\Delta g'_{\rm req}(\nu) = \alpha_g \Delta g_{\rm req}(\nu)$ and derive that $\alpha_g \approx 4.4$ allows us to match the total gain systematic budget, $\Delta r = 6.5 \times 10^{-6}$. We highlight that, similarly to what was done in ref. [52], this analysis has been performed within a simple foreground modelling frame, without any spatial variability of the polarised dust and synchrotron spectral parameters.

We therefore repeated the analysis with the injection of gain calibration uncertainties (according to the requirements derived for the simplest sky model) to all channels simultaneously when spatial variations of foreground spectral properties are assumed in the sky model. In order to account for these spatial variations of foregrounds spectral parameters, we used both the ideal and realistic approaches of the MC-NILC algorithm, described in section 5.2.1, as the component-separation technique. We found that for the ideal version of MC-NILC, we are able to fulfill the total gain systematics budget for both the `d1s1` and `d10s5` sky models (Δ below $\Delta r = 6.5 \times 10^{-6}$ by a factor of 3 and 1.3, respectively). In the frame of realistic

JCAP01(2025)019

MC-NILC and for both sky models, we can marginalise over the foreground residuals, since in these specific cases, the estimation of r is distorted by the foreground-residual bias. As already commented in section 5.2.1, marginalisation over foreground residuals will be one of the steps of any realistic estimate of the tensor-to-scalar ratio from *LiteBIRD* data. In the case of the application of realistic MC-NILC, we found that the value of Δ remains below the total gain systematics budget for the `d1s1` sky model, while slightly exceeding it for `d10s5` (about 2 times larger). We thus estimated the factor ${\alpha_g}^{\mathrm{s5,d10}}$ by which we should diminish the requirements to match the assigned gain-systematics budget when the realistic MC-NILC method is applied on `d10s5` simulations and obtained ${\alpha_g}^{\mathrm{s5,d10}} \approx 1.8$. Therefore, given the dependence of the gain-calibration uncertainties on the assumed sky model, we can only set a range for the requirements on gain calibration of each frequency channel. The lower bounds were found considering a simplistic (optimistic) scenario (NILC with `d0s0` foregrounds) and are reported in table 2, while the upper limits were obtained by simply rescaling the optimistic ones by a factor ${\alpha_g}^{\mathrm{s5,d10}} \approx 1.8$, as derived in a more pessimistic case where the `d10s5` sky model is assumed.

The effectiveness of the more realistic MC-NILC approach can be augmented by combining it with alternative (semi-)blind approaches, such as the (optimised) constrained-moment ILC (o)cMILC [77, 78]. These methods aim at deprojecting foreground moments in order to retrieve a minimum foreground variance solution, being particularly effective on intermediate and small angular scales. Therefore, future studies may be conducted with an improved blind component-separation approach that takes advantage of both MC-NILC and (o)cMILC implementation at different angular scales. The procedure presented in this paper is quite general and could eventually be applied to any kind of systematic effect, such as beam far sidelobes [79], for which requirements have been derived in the context of *LiteBIRD*, finding very stringent requirements on the accuracy of the beam knowledge, especially at synchrotron- and dust-dominated frequencies.

As a concluding remark, in this analysis, we assessed the impact of an imperfect relative polarisation gain calibration on the tensor-to-scalar ratio estimation, without accounting for the possible coupling of this with other types of systematic effect. For example, it is known that, the presence of a non-ideal rotating half-wave plate [57] can potentially induce a mixing of the Stokes parameters (specifically, intensity-to-polarisation leakage), directly affecting gain variations and therefore our requirements. The impact of the combination of all instrumental systematic effects on component separation through an end-to-end analysis is left for future work.

Acknowledgments

This work is supported in Japan by ISAS/JAXA for Pre-Phase A2 studies, by the acceleration pro- gram of JAXA research and development directorate, by the World Premier International Research Center Initiative (WPI) of MEXT, by the JSPS Core-to-Core Program of A. Advanced Research Networks, and by JSPS KAKENHI Grant Numbers JP15H05891, JP17H01115, and JP17H01125. The Canadian contribution is supported by the Canadian Space Agency. The French LiteBIRD phase A contribution is supported by the Centre National d'Etudes Spatiale (CNES), by the Centre National de la Recherche Scientifique

JCAP01(2025)019

(CNRS), and by the Commissariat á l'Energie Atomique (CEA). The German participation in LiteBIRD is supported in part by the Excellence Cluster ORIGINS, which is funded by the Deutsche Forschungsgemeinschaft (DFG, German Research Foundation) under Germany's Excellence Strategy (Grant No. EXC-2094–390783311). The Italian LiteBIRD phase A contribution is supported by the Italian Space Agency (ASI Grants No. 2020-9-HH.0 and 2016-24-H.1-2018), the National Institute for Nuclear Physics (INFN) and the National Institute for Astrophysics (INAF). Norwegian participation in LiteBIRD is supported by the Research Council of Norway (Grant No. 263011) and has received funding from the European Research Council (ERC) under the Horizon 2020 Research and Innovation Programme (Grant agreement No. 772253 and 819478). The Spanish LiteBIRD phase A contribution is supported by the Spanish Agencia Estatal de Investigación (AEI), project refs. PID2019-110610RB-C21, PID2020-120514GB-I00, ProID2020010108 and ICTP20210008. Funds that support contributions from Sweden come from the Swedish National Space Agency (SNSA/Rymdstyrelsen) and the Swedish Research Council (Reg. no. 2019-03959). The U.S. contribution is supported by NASA grant no. 80NSSC18K0132. This work has also received funding by the European Union's Horizon 2020 research and innovation programme under grant agreement no. 101007633 CMB-Inflate. It also received partial support from the Italian Space Agency LiteBIRD Project (ASI Grants No. 2020-9-HH.0 and 2016-24-H.1-2018), as well as the LiteBIRD Initiative of the National Institute for Nuclear Phyiscs, and the RadioForegroundsPlus Project HORIZON-CL4-2023-SPACE-01, GA 101135036. This work benefited from computational resources provided by the National Energy Research Scientific Computing Center (NERSC), managed by the Lawrence Berkeley National Laboratory for U.S. Department of Energy.

JCAP01(2025)019

References

[1] A.A. Penzias and R.W. Wilson, *A Measurement of excess antenna temperature at* 4080 *Mc/s*, *Astrophys. J.* **142** (1965) 419 [INSPIRE].

[2] C.H. Lineweaver, L. Tenorio, G.F. Smoot, P. Keegstra, A.J. Banday and P. Lubin, *The dipole observed in the COBE DMR four-year data*, *Astrophys. J.* **470** (1996) 38 [astro-ph/9601151] [INSPIRE].

[3] C.L. Bennett et al., *Nine-Year Wilkinson Microwave Anisotropy Probe (WMAP) Observations: Final Maps and Results*, *Astrophys. J. Suppl.* **208** (2013) 20 [arXiv:1212.5225] [INSPIRE].

[4] Planck collaboration, *Planck 2013 results. I. Overview of products and scientific results*, *Astron. Astrophys.* **571** (2014) A1 [arXiv:1303.5062] [INSPIRE].

[5] Planck collaboration, *Planck 2015 results. I. Overview of products and scientific results*, *Astron. Astrophys.* **594** (2016) A1 [arXiv:1502.01582] [INSPIRE].

[6] Planck collaboration, *Planck 2018 results. I. Overview and the cosmological legacy of Planck*, *Astron. Astrophys.* **641** (2020) A1 [arXiv:1807.06205] [INSPIRE].

[7] Boomerang collaboration, *First results from the BOOMERanG experiment*, in the proceedings of the *Conference on Cosmology and Particle Physics (CAPP 2000)*, Verbier, Switzerland, 17–28 July 2000, R. Durrer, J. Garcia-Bellido and M. Shaposhnikov eds., AIP Publishing, Melville, NY, U.S.A. (2001) [*AIP Conf. Proc.* **555** (2001) 85] [astro-ph/0011469] [INSPIRE].

[8] SPT-3G collaboration, *Measurement of the CMB temperature power spectrum and constraints on cosmology from the SPT-3G 2018 TT, TE, and EE dataset*, *Phys. Rev. D* **108** (2023) 023510 [arXiv:2212.05642] [INSPIRE].

[9] M.S. Madhavacheril et al., *The Atacama Cosmology Telescope: DR6 Gravitational Lensing Map and Cosmological Parameters*, *Astrophys. J.* **962** (2024) 113 [arXiv:2304.05203] [INSPIRE].

[10] A.H. Guth, *The Inflationary Universe: A Possible Solution to the Horizon and Flatness Problems*, *Phys. Rev. D* **23** (1981) 347 [INSPIRE].

[11] M. Kamionkowski, A. Kosowsky and A. Stebbins, *A Probe of primordial gravity waves and vorticity*, *Phys. Rev. Lett.* **78** (1997) 2058 [astro-ph/9609132] [INSPIRE].

[12] W. Hu and M.J. White, *A CMB polarization primer*, *New Astron.* **2** (1997) 323 [astro-ph/9706147] [INSPIRE].

[13] U. Seljak and M. Zaldarriaga, *Signature of gravity waves in polarization of the microwave background*, *Phys. Rev. Lett.* **78** (1997) 2054 [astro-ph/9609169] [INSPIRE].

[14] PLANCK collaboration, *Planck 2018 results. X. Constraints on inflation*, *Astron. Astrophys.* **641** (2020) A10 [arXiv:1807.06211] [INSPIRE].

[15] M. Tristram et al., *Improved limits on the tensor-to-scalar ratio using BICEP and Planck data*, *Phys. Rev. D* **105** (2022) 083524 [arXiv:2112.07961] [INSPIRE].

[16] G. Galloni, N. Bartolo, S. Matarrese, M. Migliaccio, A. Ricciardone and N. Vittorio, *Updated constraints on amplitude and tilt of the tensor primordial spectrum*, *JCAP* **04** (2023) 062 [arXiv:2208.00188] [INSPIRE].

[17] POLARBEAR collaboration, *Measurement of the Cosmic Microwave Background Polarization Lensing Power Spectrum with the POLARBEAR experiment*, *Phys. Rev. Lett.* **113** (2014) 021301 [arXiv:1312.6646] [INSPIRE].

[18] BICEP/KECK collaboration, *Measurements of Degree-Scale B-mode Polarization with the BICEP/Keck Experiments at South Pole*, in the proceedings of the *53rd Rencontres de Moriond on Cosmology*, La Thuile, Italy, 17–24 March 2018, arXiv:1807.02199 [INSPIRE].

[19] A. Blanchard and J. Schneider, *Gravitational lensing effect on the fluctuations of the cosmic background radiation*, *Astron. Astrophys.* **184** (1987) 1.

[20] M. Zaldarriaga and U. Seljak, *Gravitational lensing effect on cosmic microwave background polarization*, *Phys. Rev. D* **58** (1998) 023003 [astro-ph/9803150] [INSPIRE].

[21] E.J. Baxter et al., *A Measurement of Gravitational Lensing of the Cosmic Microwave Background by Galaxy Clusters Using Data from the South Pole Telescope*, *Astrophys. J.* **806** (2015) 247 [arXiv:1412.7521] [INSPIRE].

[22] B.D. Sherwin et al., *Two-season Atacama Cosmology Telescope polarimeter lensing power spectrum*, *Phys. Rev. D* **95** (2017) 123529 [arXiv:1611.09753] [INSPIRE].

[23] N. Krachmalnicoff, C. Baccigalupi, J. Aumont, M. Bersanelli and A. Mennella, *Characterization of foreground emission on degree angular scales for CMB B-mode observations — Thermal dust and synchrotron signal from Planck and WMAP data*, *Astron. Astrophys.* **588** (2016) A65 [arXiv:1511.00532] [INSPIRE].

[24] G.B. Rybicki and A.P. Lightman, *Radiative Processes in Astrophysics*, Wiley, New York, NY (1985) [DOI:10.1002/9783527618170] [INSPIRE].

JCAP01(2025)019

[25] N. Macellari, E. Pierpaoli, C. Dickinson and J.E. Vaillancourt, *Galactic foreground contributions to the WMAP5 maps*, *Mon. Not. Roy. Astron. Soc.* **418** (2011) 888 [arXiv:1108.0205] [INSPIRE].

[26] C. Dickinson, M.W. Peel and M. Vidal, *New constraints on the Polarization of Anomalous Microwave Emission in nearby molecular clouds*, *Mon. Not. Roy. Astron. Soc. Lett.* **418** (2011) L35 [arXiv:1108.0308] [INSPIRE].

[27] D. Herman et al., *BEYONDPLANCK — XV. Limits on large-scale polarized anomalous microwave emission from Planck LFI and WMAP*, *Astron. Astrophys.* **675** (2023) A15 [arXiv:2201.03530] [INSPIRE].

[28] R. Génova-Santos et al., *QUIJOTE scientific results — II. Polarisation measurements of the microwave emission in the Galactic molecular complexes W43 and W47 and supernova remnant W44*, *Mon. Not. Roy. Astron. Soc.* **464** (2017) 4107 [arXiv:1605.04741] [INSPIRE].

[29] R. González-González et al., *QUIJOTE scientific results — XVIII. New constraints on the polarization of the Anomalous Microwave Emission in bright Galactic regions: ρ Ophiuchi, Perseus and W43*, arXiv:2409.03418 [INSPIRE].

[30] G. Puglisi, G. Fabbian and C. Baccigalupi, *A 3D model for carbon monoxide molecular line emission as a potential cosmic microwave background polarization contaminant*, *Mon. Not. Roy. Astron. Soc.* **469** (2017) 2982 [arXiv:1701.07856] [INSPIRE].

[31] Planck collaboration, *Planck 2018 results. XI. Polarized dust foregrounds*, *Astron. Astrophys.* **641** (2020) A11 [arXiv:1801.04945] [INSPIRE].

[32] V. Pelgrims et al., *Evidence for Line-of-Sight Frequency Decorrelation of Polarized Dust Emission in Planck Data*, *Astron. Astrophys.* **647** (2021) A16 [arXiv:2101.09291] [INSPIRE].

[33] R. Skalidis et al., *Local measurements of the mean interstellar polarization at high Galactic latitudes*, *Astron. Astrophys.* **616** (2018) A52 [arXiv:1802.04305] [INSPIRE].

[34] Planck collaboration, *Planck 2018 results. IV. Diffuse component separation*, *Astron. Astrophys.* **641** (2020) A4 [arXiv:1807.06208] [INSPIRE].

[35] H.K. Eriksen, J.B. Jewell, C. Dickinson, A.J. Banday, K.M. Górski and C.R. Lawrence, *Joint Bayesian component separation and CMB power spectrum estimation*, *Astrophys. J.* **676** (2008) 10 [arXiv:0709.1058] [INSPIRE].

[36] R. Stompor, S.M. Leach, F. Stivoli and C. Baccigalupi, *Maximum Likelihood algorithm for parametric component separation in CMB experiments*, *Mon. Not. Roy. Astron. Soc.* **392** (2009) 216 [arXiv:0804.2645] [INSPIRE].

[37] E. de la Hoz, P. Vielva, R.B. Barreiro and E. Martínez-González, *On the detection of CMB B-modesfrom ground at low frequency*, *JCAP* **06** (2020) 006 [arXiv:2002.12206] [INSPIRE].

[38] S. Azzoni, M.H. Abitbol, D. Alonso, A. Gough, N. Katayama and T. Matsumura, *A minimal power-spectrum-based moment expansion for CMB B-mode searches*, *JCAP* **05** (2021) 047 [arXiv:2011.11575] [INSPIRE].

[39] L. Vacher, J. Aumont, L. Montier, S. Azzoni, F. Boulanger and M. Remazeilles, *Moment expansion of polarized dust SED: A new path towards capturing the CMB B-modes with LiteBIRD*, *Astron. Astrophys.* **660** (2022) A111 [arXiv:2111.07742] [INSPIRE].

[40] M. Galloway et al., *BEYONDPLANCK — III. Commander3*, *Astron. Astrophys.* **675** (2023) A3 [arXiv:2201.03509] [INSPIRE].

JCAP01(2025)019

[41] J. Delabrouille, J.F. Cardoso, M. Le Jeune, M. Betoule, G. Fay and F. Guilloux, *A full sky, low foreground, high resolution CMB map from WMAP*, *Astron. Astrophys.* **493** (2009) 835 [arXiv:0807.0773] [INSPIRE].

[42] R. Vio and P. Andreani, *"Internal Linear Combination" method for the separation of CMB from Galactic foregrounds in the harmonic domain*, arXiv:0811.4277 [INSPIRE].

[43] M. Remazeilles, J. Delabrouille and J.-F. Cardoso, *Foreground component separation with generalised ILC*, *Mon. Not. Roy. Astron. Soc.* **418** (2011) 467 [arXiv:1103.1166] [INSPIRE].

[44] M. Remazeilles, J. Delabrouille and J.-F. Cardoso, *CMB and SZ effect separation with Constrained Internal Linear Combinations*, *Mon. Not. Roy. Astron. Soc.* **410** (2011) 2481 [arXiv:1006.5599] [INSPIRE].

[45] A. Carones et al., *Multiclustering needlet ILC for CMB B-mode component separation*, *Mon. Not. Roy. Astron. Soc.* **525** (2023) 3117 [arXiv:2212.04456] [INSPIRE].

[46] M. Tegmark, A. de Oliveira-Costa and A. Hamilton, *A high resolution foreground cleaned CMB map from WMAP*, *Phys. Rev. D* **68** (2003) 123523 [astro-ph/0302496] [INSPIRE].

[47] M. Hazumi et al., *LiteBIRD: A Satellite for the Studies of B-Mode Polarization and Inflation from Cosmic Background Radiation Detection*, *J. Low Temp. Phys.* **194** (2019) 443 [INSPIRE].

[48] LITEBIRD collaboration, *Probing Cosmic Inflation with the LiteBIRD Cosmic Microwave Background Polarization Survey*, *Prog. Theor. Exp. Phys.* **2023** (2023) 042F01 [arXiv:2202.02773] [INSPIRE].

[49] LITEBIRD collaboration, *The LiteBIRD mission to explore cosmic inflation*, in the proceedings of the *SPIE Astronomical Telescopes + Instrumentation 2024*, Yokohama, Japan, 16–21 June 2024, *Proc. SPIE* **13092** (2024) 1309228 [arXiv:2406.02724] [INSPIRE].

[50] S. Basak and J. Delabrouille, *A needlet ILC analysis of WMAP 7-year polarisation data: CMB polarisation power spectra*, *Mon. Not. Roy. Astron. Soc.* **435** (2013) 18 [arXiv:1204.0292] [INSPIRE].

[51] A. Carones, M. Migliaccio, D. Marinucci and N. Vittorio, *Analysis of Needlet Internal Linear Combination performance on B-mode data from sub-orbital experiments*, *Astron. Astrophys.* **677** (2023) A147 [arXiv:2208.12059] [INSPIRE].

[52] T. Ghigna, T. Matsumura, G. Patanchon, H. Ishino and M. Hazumi, *Requirements for future CMB satellite missions: photometric and band-pass response calibration*, *JCAP* **11** (2020) 030 [arXiv:2004.11601] [INSPIRE].

[53] E. Gjerløw et al., *BEYONDPLANCK — VII. Bayesian estimation of gain and absolute calibration for cosmic microwave background experiments*, *Astron. Astrophys.* **675** (2023) A7 [arXiv:2011.08082] [INSPIRE].

[54] Y. Sekimoto et al., *Concept Design of Low Frequency Telescope for CMB B-mode Polarization satellite LiteBIRD*, *Proc. SPIE* **11453** (2020) 1145310 [arXiv:2101.06342] [INSPIRE].

[55] L. Montier et al., *Overview of the Medium and High Frequency Telescopes of the LiteBIRD satellite mission*, in the proceedings of the *Space Telescopes and Instrumentation 2020: Optical, Infrared, and Millimeter Wave*, proceedings of the *SPIE Astronomical Telescopes + Instrumentation*, Online Only, CA, U.S.A., 14–18 December 2020, *Proc. SPIE* **11443** (2020) 114432G [arXiv:2102.00809] [INSPIRE].

[56] S. Giardiello et al., *Detailed study of HWP non-idealities and their impact on future measurements of CMB polarization anisotropies from space*, *Astron. Astrophys.* **658** (2022) A15 [*Erratum ibid.* **671** (2023) C1] [arXiv:2106.08031] [INSPIRE].

JCAP01(2025)019

[57] M. Monelli, E. Komatsu, T. Ghigna, T. Matsumura, G. Pisano and R. Takaku, *Impact of half-wave plate systematics on the measurement of CMB B-mode polarization*, *JCAP* **05** (2024) 018 [arXiv:2311.07999] [INSPIRE].

[58] G. Patanchon, H. Imada, H. Ishino and T. Matsumura, *Effect of instrumental polarization with a half-wave plate on the B-mode signal: prediction and correction*, *JCAP* **04** (2024) 074 [arXiv:2308.00967] [INSPIRE].

[59] A. Kogut et al., *Three-Year Wilkinson Microwave Anisotropy Probe (WMAP) Observations: Foreground Polarization*, *Astrophys. J.* **665** (2007) 355 [arXiv:0704.3991] [INSPIRE].

[60] M.-A. Miville-Deschênes et al., *Separation of anomalous and synchrotron emissions using WMAP polarization data*, *Astron. Astrophys.* **490** (2008) 1093 [arXiv:0802.3345] [INSPIRE].

[61] U. Fuskeland, I.K. Wehus, H.K. Eriksen and S.K. Næss, *Spatial variations in the spectral index of polarized synchrotron emission in the 9-yr WMAP sky maps*, *Astrophys. J.* **790** (2014) 104 [arXiv:1404.5323] [INSPIRE].

[62] N. Krachmalnicoff et al., *S-PASS view of polarized Galactic synchrotron at 2.3 GHz as a contaminant to CMB observations*, *Astron. Astrophys.* **618** (2018) A166 [arXiv:1802.01145] [INSPIRE].

[63] PLANCK collaboration, *Planck 2018 results. V. CMB power spectra and likelihoods*, *Astron. Astrophys.* **641** (2020) A5 [arXiv:1907.12875] [INSPIRE].

[64] A. Lewis, A. Challinor and A. Lasenby, *Efficient computation of CMB anisotropies in closed FRW models*, *Astrophys. J.* **538** (2000) 473 [astro-ph/9911177] [INSPIRE].

[65] M. Zaldarriaga and U. Seljak, *An all sky analysis of polarization in the microwave background*, *Phys. Rev. D* **55** (1997) 1830 [astro-ph/9609170] [INSPIRE].

[66] P. Ade et al., *The Simons Observatory: Science goals and forecasts*, *JCAP* **02** (2019) 056 [arXiv:1808.07445] [INSPIRE].

[67] J. Dick, M. Remazeilles and J. Delabrouille, *Impact of calibration errors on CMB component separation using FastICA and ILC*, *Mon. Not. Roy. Astron. Soc.* **401** (2010) 1602 [arXiv:0907.3105] [INSPIRE].

[68] C.L. Bennett et al., *First year Wilkinson Microwave Anisotropy Probe (WMAP) observations: Foreground emission*, *Astrophys. J. Suppl.* **148** (2003) 97 [astro-ph/0302208] [INSPIRE].

[69] F.J. Narcowich, P. Petrushev and J.D. Ward, *Localized Tight Frames on Spheres*, *SIAM J. Math. Anal.* **38** (2006) 574.

[70] D. Marinucci et al., *Spherical Needlets for CMB Data Analysis*, *Mon. Not. Roy. Astron. Soc.* **383** (2008) 539 [arXiv:0707.0844] [INSPIRE].

[71] D. Geller and A. Mayeli, *Continuous Wavelets on Compact Manifolds*, *Math. Z.* **262** (2009) 895 [arXiv:0811.4440].

[72] K.M. Górski et al., *HEALPix — A Framework for high resolution discretization, and fast analysis of data distributed on the sphere*, *Astrophys. J.* **622** (2005) 759 [astro-ph/0409513] [INSPIRE].

[73] S. Hamimeche and A. Lewis, *Likelihood Analysis of CMB Temperature and Polarization Power Spectra*, *Phys. Rev. D* **77** (2008) 103013 [arXiv:0801.0554] [INSPIRE].

[74] N. Katayama and E. Komatsu, *Simple foreground cleaning algorithm for detecting primordial B-mode polarization of the cosmic microwave background*, *Astrophys. J.* **737** (2011) 78 [arXiv:1101.5210] [INSPIRE].

JCAP01(2025)019

[75] A. Mangilli et al., *Dust moments: towards a new modelling of the galactic dust emission for CMB B-modes analysis*, *Astron. Astrophys.* **647** (2021) A52 [arXiv:1912.09567] [INSPIRE].

[76] A. Ritacco et al., *Dust polarization spectral dependence from Planck HFI data — Turning point for cosmic microwave background polarization-foreground modeling*, *Astron. Astrophys.* **670** (2023) A163 [arXiv:2206.07671] [INSPIRE].

[77] M. Remazeilles, A. Rotti and J. Chluba, *Peeling off foregrounds with the constrained moment ILC method to unveil primordial CMB B-modes*, *Mon. Not. Roy. Astron. Soc.* **503** (2021) 2478 [arXiv:2006.08628] [INSPIRE].

[78] A. Carones and M. Remazeilles, *Optimization of foreground moment deprojection for semi-blind CMB polarization reconstruction*, *JCAP* **06** (2024) 018 [arXiv:2402.17579] [INSPIRE].

[79] C. Leloup et al., *Impact of beam far side-lobe knowledge in the presence of foregrounds for LiteBIRD*, *JCAP* **06** (2024) 011 [arXiv:2312.09001] [INSPIRE].

JCAP01(2025)019